journal of the mechanical behavior of biomedical materials 134 (2022) 105409

Contents lists available at ScienceDirect

Journal of the Mechanical Behavior of Biomedical Materials

journal homepage: www.elsevier.com/locate/jmbbm

Mechanical performance of additively manufactured cobalt-chromium-molybdenum auxetic meta-biomaterial bone scaffolds

Chameekara T. Wanniarachchi [a,b], Arun Arjunan [a,b,*], Ahmad Baroutaji [a,b], Manpreet Singh [a,b]

[a] Additive Manufacturing of Functional Materials (AMFM) Research Group, Centre for Engineering Innovation and Research, University of Wolverhampton, Telford Campus, Telford, TF2 9NT, UK

[b] School of Engineering, Computing and Mathematical Sciences, Faculty of Science and Engineering, University of Wolverhampton, Telford Campus, Telford, TF2 9NT, UK

ARTICLE INFO

Keywords:
Additive manufacturing
Laser-powder bed fusion
Metamaterials
Bone scaffolds
Meta-biomaterial

ABSTRACT

Auxetic meta-biomaterials offer unconventional strain behaviour owing to their negative Poisson's ratio ($-\upsilon$) leading to deformation modes and mechanical properties different to traditional cellular biomaterials. This can lead to favourable outcomes for load-bearing tissue engineering constructs such as bone scaffolds. Emerging early-stage studies have shown the potential of auxetic architecture in increasing cell proliferation and tissue reintegration owing to their $-\upsilon$. However, research on the development of CoCrMo auxetic meta-biomaterials including bone scaffolds or implants is yet to be reported. In this regard, this paper proposes a potential framework for the development of auxetic meta-biomaterials that can be printed on demand while featuring porosity requirements suitable for load-bearing bone scaffolds. Overall, the performance of five CoCrMo auxetic meta-biomaterial scaffolds characterised under two scenarios for their potential to offer near-zero and high negative Poisson's ratio is demonstrated. Ashby's criterion followed by prototype testing was employed to evaluate the mechanical performance and failure modes of the auxetic meta-biomaterial scaffolds under uniaxial compression. The best performing scaffold architectures are identified through a multi-criteria decision-making procedure combining 'analytic hierarchy process' (AHP) and 'technique for order of preference by similarity to ideal solution' (TOPSIS). The results found the Poisson's ratio for the meta-biomaterial architectures to be in the range of −0.1 to −0.24 at a porosity range of 73–82%. It was found that the meta-biomaterial scaffold (AX1) that offered the highest auxeticity also showed the highest elastic modulus, yield, and ultimate strength of 1.66 GPa, 56 MPa and 158 MPa, respectively. The study demonstrates that the elastic modulus, yield stress, and Poisson's ratio of auxetic meta-biomaterials are primarily influenced by the underlying meta-cellular architecture followed by relative density offering a secondary influence.

1. Introduction

Developing biomaterials for tissue reconstruction has been largely based on the synthesis of new biopolymers, composites, or alloys (Rahmani et al., 2022; Davoodi et al., 2022). However, recent development in digital fabrication has enabled an alternative paradigm where biomaterials can be conceived for targeted mechanical and biological properties (Ganjian et al., 2022; Zhang et al., 2022a; Kluyskens et al., 2022). In most cases, the precise control over the properties is enabled by carefully conceived cellular architecture at the sub-micron scale. Zadpoor (2020) describes this approach of developing constructs with novel functionalities as 'rational design'. Rationally designed materials that offer control over their bulk material behaviour while facilitating new or functional properties can be referred to as metamaterial. When such metamaterial architectures are being developed for biomedical applications, they are termed meta-biomaterials (Kolken et al., 2022a, 2022b; Baroutaji et al., 2022).

The focus of this research is on the development of a specific class of meta-biomaterials that shrinks laterally in response to axial compression resulting in a negative Poisson's ratio ($-\upsilon$). Such architectures are commonly referend to as auxetic meta-biomaterials signified by $-\upsilon$, that may offer enhanced functionality for tissue generation. Auxetic structures have potential in the biomedical industry due to their $-\upsilon$ (Scarpa, 2008). Auxetic bone scaffolds, dental implants, neck braces,

* Corresponding author. Additive Manufacturing of Functional Materials (AMFM) research group, Centre for Engineering Innovation and Research, University of Wolverhampton, Telford Campus, Telford, TF2 9NT, UK.
E-mail address: a.arjunan@wlv.ac.uk (A. Arjunan).

https://doi.org/10.1016/j.jmbbm.2022.105409
Received 27 May 2022; Received in revised form 22 July 2022; Accepted 30 July 2022
Available online 12 August 2022

dilators, cage spacers for spine surgery and the femoral component of the total hip implant are some of the areas that are being experimented with. Baker (2013) showed the potential application of auxetic meta-biomaterials for the reconstruction of intervertebral discs showing that a $-\upsilon$ would be helpful to prevent disc degeneration disease. In particular, Baker argued that the decrease in the horizontal motion of the intervertebral disc reduces the impact on nerves.

Several biological tissues have been reported in the literature (Mardling et al., 2020; Williams and Lewis, 1982; Kim et al., 2021) as featuring either fully or partially $-\upsilon$ demonstrating auxetic behaviour. The auxetic behaviour of biological tissues affects both their loading environment and tissue regeneration. Generally, the attachment of host tissue to a biomaterial is influenced by the functional interface between the biomaterial and the tissue. As such tissue engineering constructs such as bone scaffolds featuring auxetic behaviour may offer enhanced opportunities for large load-bearing tissue reconstruction such as in the case of critical size bone defects (CSBD).

According to Mardling et al. (2020), auxetic structures could be used in a variety of tissue engineering and biomedical applications. The femoral component for complete hip replacements was designed and fabricated using auxetic structures created via additive manufacturing (Abdelaal and Darwish, 2012; Hazlehurst et al., 2014). Choi et al. (2016) investigated the use of auxetic PLGA (Poly Lactic-*co*-Glycolic Acid) scaffolds and their effectiveness in increasing the number of bone cells under compressive stimulation. It was shown that the negative Poisson's ratio enhanced compressive stimulation in all directions resulting in an accelerated bone cell response increasing the number of bone cells being regenerated (Choi et al., 2016). The study conducted by Kolken et al. (2020) has also shown that titanium auxetic meta-biomaterials offer functionalities suitable for bone implant applications.

The rise in digital manufacturing (Warner et al., 2017; Jin et al., 2021; Arjunan et al., 2020a) techniques such as additive manufacturing (AM) offer significant potential for engineering bone scaffolds featuring complex porous architecture that can lead to auxetic behaviour. Unlike traditional methods, AM allows for a great deal of flexibility and complexity in the creation of porous materials offering new functionalities (Joseph et al., 2021; Robinson et al., 2021; Arjunan et al., 2021a, 2021b; Zhang et al., 2020, 2022b). The adoption of AM in the generation of auxetic structures for tissue reconstruction can lead to a personalised and cost-effective architecture that is fit for purpose.

Despite the increasing literature on AM, the development of auxetic meta-biomaterials in cobalt-chromium-molybdenum (CoCrMo) superalloy are yet to be demonstrated. In this regard, the research investigates the use of laser-powder bed fusion (L-PBF) additive manufacturing to develop CoCrMo auxetic bone scaffolds that can offer near-zero and high $-\upsilon$. Five open porous CoCrMo auxetic scaffold designs are conceived at a porosity range of 80–87% fabricated using L-PBF using. The print quality of the scaffolds was analysed using scanning electron microscopy (SEM) to characterise the influence of L-PBF on the dimensional accuracy of the scaffolds. Subsequently, physical tests and finite element modelling is used to explain the mechanical behaviour of the L-PBF CoCrMo auxetic scaffolds. The physical test data was also used to evaluate the suitability of Gibson and Ashby models and the finite element method (FEM) in predicting the mechanical performance of CoCrMo auxetic scaffolds.

The study also introduces a methodology to identify auxetic bone scaffolds considering multi-criteria decision making. A combination of two techniques, namely the 'technique for order preference by similarity to ideal solutions' (TOPSIS) and the 'analytic hierarchy process' (AHP) are considered. The hybrid technique is used to identify the best auxetic scaffold under two scenarios, which can offer specific advantages. The first scenario looks at identifying the auxetic scaffold design that offers a near-zero $-\upsilon$ while satisfying five different criteria required for bone scaffolds. The second scenario identifies the auxetic scaffolds that offer the highest $-\upsilon$ while offering suitable performance for other selected parameters. This is the first research to bring forward the combined AHP and TOPSIS methodology within the context of auxetic scaffold design to aid decision-making. Altogether, the study proposes a methodology for conceiving and selecting CoCrMo auxetic meta-biomaterial bone scaffolds that can offer targeted functionalities and mechanical behaviour suitable for the application to critical size bone defects.

2. Methodology

2.1. Auxetic scaffold design

Cellular materials are generally conceived with the help of repeating unit cells (UCs) that feature as symmetry elements (Baroutaji et al., 2019; Ashby, 2006). The macroscopic properties (stiffness and strength) of the resulting solid material are informed by both the bulk material and the cellular architecture (Bauer et al., 2014; Yang et al., 2002; Tolochko et al., 2002; Barbas et al., 2012). This study presents five different auxetic UCs as shown in Fig. 1 which are used as the foundation for the meta-biomaterial scaffold design. SolidWorks (Dassault Systèmes) 2019 CAD package was the software of choice to conceive and generate all the meta-biomaterial architectures. A considered approach was taken in the selection of unit cells to ensure interconnected porosity which is a requirement for tissue engineering scaffolds. The unit cells were designed with limited overhangs to avoid extensive support requirements during the laser-powder bed fusion process (Arjunan et al., 2020b). Each unit cell (UC1-UC5) was conceived to fit in a $2 \times 2 \times 2$ mm cube at an 8 mm^3 bulk volume. The strut thickness was designed in such a way as to measure 0.3 mm when assembled into a lattice architecture.

The porous architecture of meta-biomaterial bone scaffold is informed by the unit cell, which dictates the mechanical properties. The linear mirroring of UCs in x, y and z coordinates resulted in five respective scaffold designs designated AX1 to AX5, as shown in Fig. 2. AX1, AX2, AX3, AX4 and AX5 used unit cells UC1 (re-entrant), UC2 (arrowhead), UC3 (modified re-entrant), UC4 (double arrowhead) and UC5 (bell-shaped) respectively. Generally, a porous scaffold will have a lower elastic modulus (E) and yield strength (σ_y) in comparison to their bulk equivalent due to the material removed by the pore voids.

For this study, CoCrMo superalloy which is chosen as the bulk material features high elastic modulus and yield strength in comparison to tibial bone. The approach offers a significant opportunity for the development of highly porous meta-cellular architecture at low stiffness suitable for the reduction of stress shielding effects at the tissue-implant interface (Arjunan et al., 2020c). The global cylindrical dimensions of the scaffolds were conceived to fit a tibial cross-section of 180.024 mm^2 leading to a scaffold radius of 7.25 mm. The dimensions are chosen such that it is suitable for the reconstruction of an adult tibial critical size defect of length 18 mm (Vance et al., 2019).

The resulting properties of the five scaffold designs are listed in Table 1. It can be seen that the scaffold properties satisfy the porosity requirements of higher than 50% for open porous bone scaffolds. The lowest and highest porosity was exhibited by scaffolds AX1 and AX4 at 80.49% and 86.74%, respectively. Once the scaffolds were fabricated, the design data was compared to physically measured porosity to characterise any deviation of the design from ideal as a result of L-PBF.

2.2. Additive manufacturing

2.2.1. CoCrMo superalloy feedstock characteristics

CoCrMo feedstock used in this research is made up of cobalt, chromium, and other metal materials, including nickel and molybdenum as summarised in Table 2. All auxetic bone scaffolds were manufactured using the Cobalt chromium MP1 supplied by EOS, which is a biocompatible CoCrMo superalloy suitable for biomedical applications. Inhouse, tests were carried out on fully dense CoCrMo tensile test coupons to characterise the bulk material properties. CoCrMo superalloys are typically used for mechanically demanding applications such as dental, artificial joints, and jewellery due to their biocompatibility (Behl

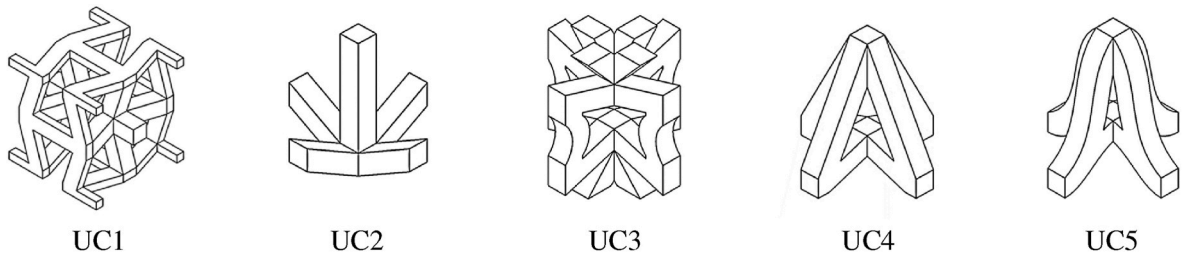

Fig. 1. Auxetic unit cells are designed for the repeating meta-cellular CoCrMo bone scaffold.

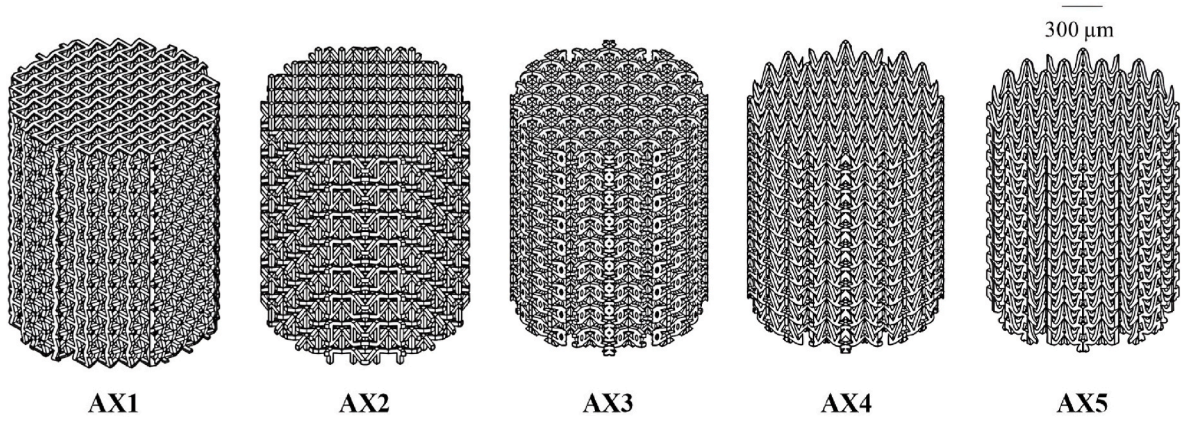

Fig. 2. Auxetic scaffold designs featuring different unit cells where UC1, UC2, UC3, UC4 and UC5 inform AX1, AX2, AX3, AX4 and AX5 respectively.

Table 1
Characteristics of the five auxetic meta-biomaterial scaffold designs conceived.

Properties	Scaffold Designs				
	AX1	AX2	AX3	AX4	AX5
Relative density (ρ_r)	0.1951	0.1614	0.1662	0.1326	0.1431
Porosity (%)	80.49	83.86	83.38	86.74	85.69

et al., 2013; dos Santos et al., 2020). The development of CoCrMo as a load-bearing biomaterial is a result of its high corrosion and wear resistance (dos Santos et al., 2020; Dobrzański and Reimann, 2011; Hazlehurst, 2014; Monroy et al., 2013). When it comes to additive manufacturing, Mantrala et al. (2015) laser processed CoCrMo and indicated that dense, metallurgically sound parts can be fabricated by optimising the laser process parameters. It was shown that high scan speed, laser power and low powder feed rate can produce CoCrMo components with good tribological, and mechanical properties (Mohamed et al., 2019).

Although CoCrMo alloys offer excellent biocompatibility, mechanical strength and corrosion resistance, titanium alloys and stainless steel are often favoured for orthopaedic applications due to their relatively low bulk material stiffness (elastic modulus). However, compressive properties of CoCrMo cellular structures with stiffness characteristics closer to the bone have been demonstrated making them an ideal biomaterial for the development of porous meta-biomaterials.

The CoCrMo powder showed a wide range of particle size distribution, where most of its particles are spherical, having a grainy surface, but some agglomerates have a smoother surface (Ada et al., Račiukaitis). For L-PBF, the properties of the feedstock such as particle shape (morphology) and size (granulometry), affect the flowability and the packing density of the powder bed (Robinson et al., 2020a, 2020b). Closely monitoring the powder characteristics also ensures both repeatability and part density when a new batch or material supplier is used. The Retsch Technology Camsizer X2 particle size analyser was used to characterise the CoCrMo powder quality.

2.2.2. Laser-powder bed fusion

The laser-powder bed fusion (LPBF) technique was used to fabricate all the auxetic scaffold designs in addition to the tensile test coupons. All samples were built using an EOS M290 featuring a laser spot size and layer thickness of 100 μm and 40 μm respectively. The optimum L-PBF process parameters used were a laser power of 290 W, a scan speed of 950 mm/s and a hatch distance of 0.11 mm. The process parameters were kept constant for the fabrication of both the tensile test specimen and the scaffolds. An Argon atmosphere was used inside the print chamber with horizontal laser beam scanning to melt the CoCrMo particles during L-PBF. The process was carried out layer-by-layer, with the build platform being lowered vertically as each layer was completed. Following that, the powder feeder and re-coater spread the powder for the next layer and the process was repeated until the complete part was built. All samples were heat-treated post-printing at 1150 °C for 6 h. Stress-relieved scaffolds and tensile test samples were removed from the base plate by using wire Electro discharge machining (EDM).

2.3. Scanning electron microscopy

Scanning Electron microscopy (SEM) is one of the most extensively

Table 2
CoCrMo alloy feedstock composition used for laser-powder bed fusion.

Elements	Co	Cr	Mo	Si	Mn	Fe	C	Ni
Composition (*wt.*%)	60–65	26–30	5–7	≤1.0	≤1.0	≤0.75	≤0.16	≤0.1

used techniques to inspect sub-micron features of additively manufactured parts due to its high magnification (Scheu and Kaplan, 2012). SEM work similarly to optical microscopes, but instead of using light, it employs a focussed stream of electrons to image the specimen and obtain information about the microscopic structure and composition (Sapti, 2019). In this work, EVO 50 SEM manufactured by Zeiss is used to characterise the morphology of CoCrMo feedstock and printed samples.

2.4. Mechanical testing

Zwick Roell 1474 materials testing machine with a maximum load capacity of 100 kN was used to conduct uniaxial tension and compression tests on the bulk material and auxetic scaffolds, respectively. Both the rights as shown in Fig. 3 featured a mounted camera to capture the cellular deformation. The tests revealed both the mechanical properties of the L-PBF processed bulk CoCrMo and the five different meta-cellular architectures satisfying BSEN ISO 13314 (International Organization for Standardization, 2011). Before commencing the experimental tests, the setup was calibrated according to BSEN ISO 7500-1 (INTERNATIONAL STANDARD verification of static, 2018).

For all tests, three samples ($n = 3$) from the same batch were analysed and the mean and standard deviation were evaluated for both the elastic modulus (E) and yield strength (σ_y) (BSI, 2016). Crosshead movement at a rate of 0.08 mm/s was set to load the test specimens to failure. The tensile test coupons were pulled to rupture and the compressive samples were loaded to a 9 mm (50% of the scaffold height) compressive deformation. The test data was visually captured through the video camera for all the specimens to characterise the failure modes.

The force-displacement data was monitored and used to evaluate the stress-strain ($\sigma - \varepsilon$) curves for all the samples. The curves were subsequently used to calculate the elastic modulus of the bulk material and the scaffold as the slope of the elastic region. The 0.2% offset method was used to determine the yield strength of the specimens from the stress-strain curves. The lateral strain values for the Poisson's ratio were measured from ImageJ using photographs taken during the elastic deformation of the scaffold. For precision, the transverse strain was computed at each lattice layer, and the average values were used, a method similar to Arjunan et al. (2020d) with Eq. (1) used to calculate the Poisson's ratio:

$$\upsilon_{yx} = -\left(\frac{\varepsilon_{lat}}{\varepsilon_y}\right) \tag{1}$$

2.5. Multi-criteria decision-making

2.5.1. Combined TOPSIS and AHP technique

Most decision-making scenarios in the real world involve conflicting criteria and objectives that are required to be simultaneously considered. When there exist multiple parameters to consider, multi-criteria decision-making (MCDM) models can be used to identify the best possible solution. MCDM models are used to achieve an optimum decision in the presence of multiple objectives and conflicting decision criteria (Raigar et al., 2020). 'Technique for order of preference by similarity to ideal solution' (TOPSIS) is one of the most widely used MCDM techniques that are capable of revealing solutions that lie close to ideal (Emovon and Oghenenyerovwho, 2020; Bertolini et al., 2020).

For scenario-based decision-making for the selection of auxetic bone scaffolds considered in this study, a combined case of TOPSIS and 'analytical hierarchy process' (AHP) is required. TOPSIS and AHP are general purpose multi-objective decision-making approaches that are suitable for a wide range of problems. Although they are employed in a hybrid fashion in this study, they are suitable for any number of parameters. In this regard, the approach presented in this paper can be extended to analyse either fewer or more than five parameters. It may be also noted that these algorithms are part of a multi-criteria decision-making methodology and as such do not inform the CAD or STL model directly. Instead, they look at the responses of the designs that are already conceived and aid decision-making as to what design performs optimally given the number and relative importance of the range of criteria. The overall implementation of the decision-making methodology using TOPSIS and AHP for the scenarios under consideration is summarised in Fig. 4.

The modelling procedures for TOPSIS are similar regardless of the number of available alternatives, thus enabling fast computations. For every alternative, the technique concurrently factors the distance from the worst solution to the best one (Sabaghi et al., 2015). The perfect positive solution involves all the good values of every rank, and the

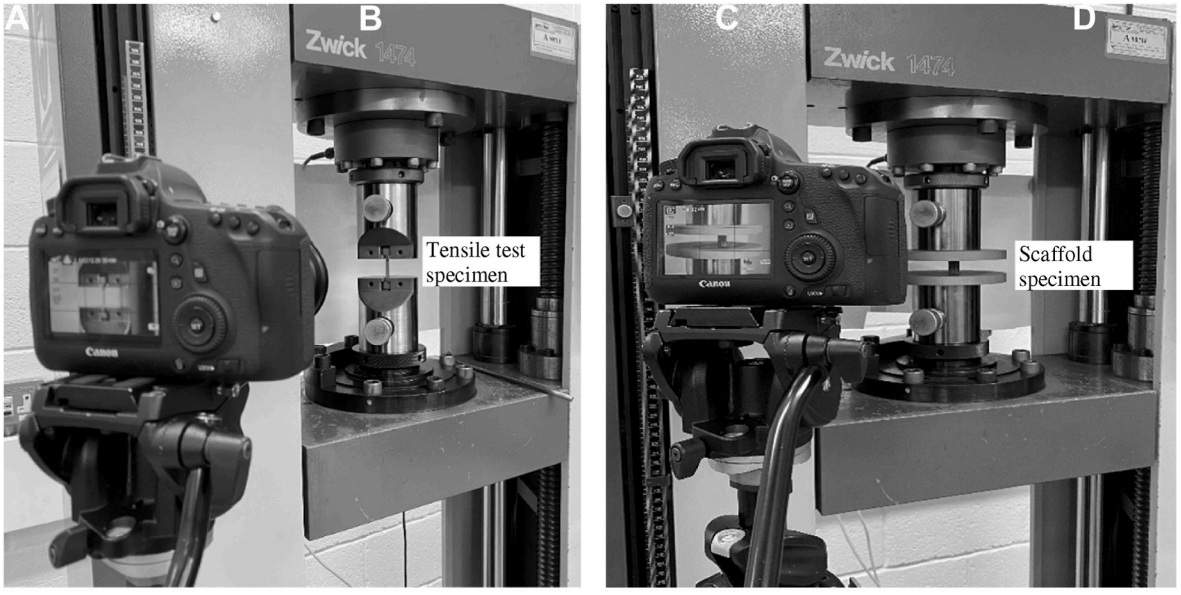

Fig. 3. Mechanical test setup showing (a) tensile test for the evaluation of CoCrMo bulk material properties and (b) compression test for mechanical properties of the auxetic scaffold.

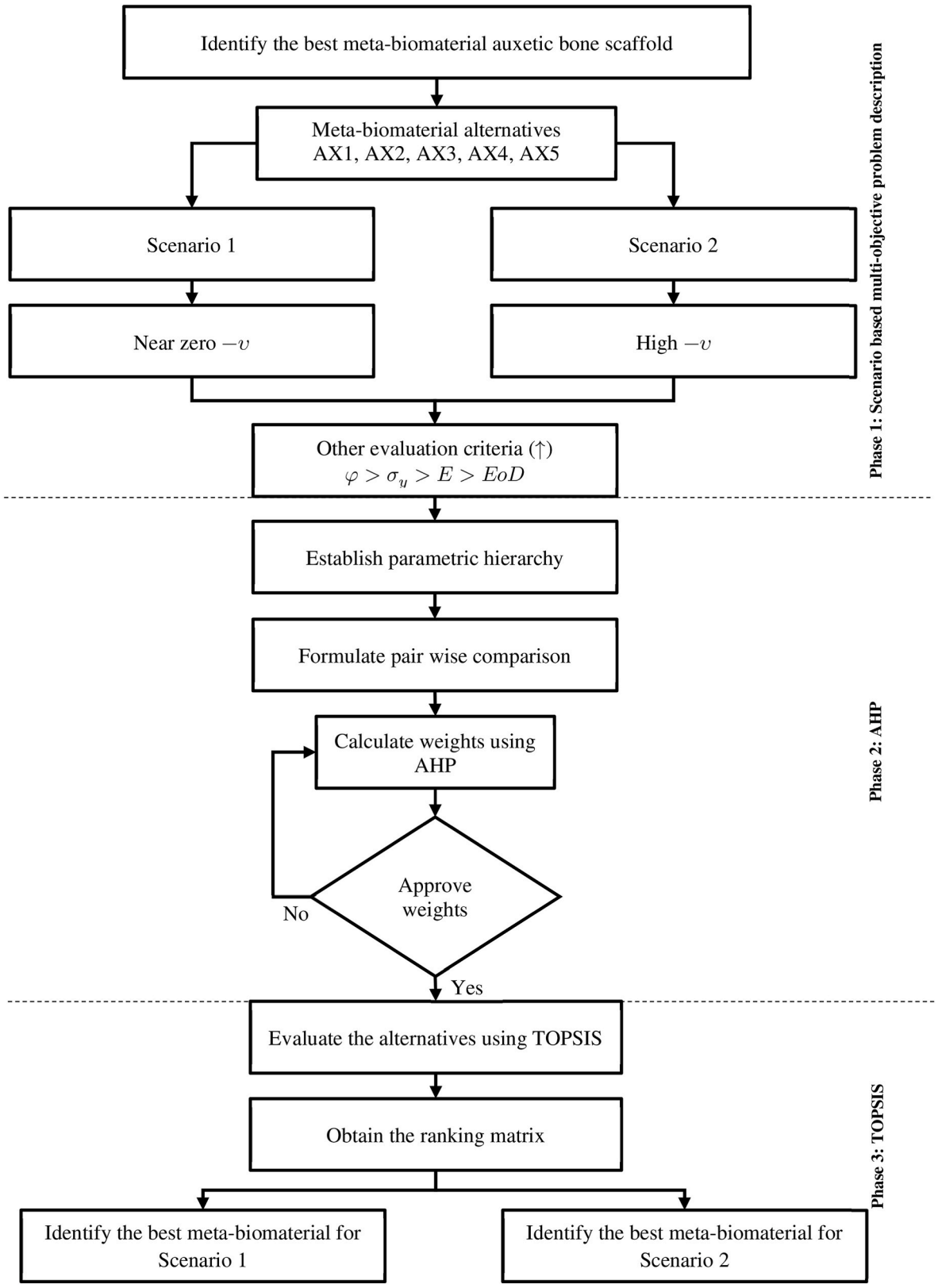

Fig. 4. Flow chart showing the scenario-based selection of near-zero and high strain auxetic meta-biomaterial bone scaffolds using combined TOPSIS and AHP decision-making methodology.

perfect negative solution involves all the worst (Rahim et al., 2018). The basic principle of the TOPSIS technique is that the optimal decision is the one that lies closest to the ideal solution (Nikkhah et al., 2019). As such, the best and worst solutions should possess a rank close to one and zero respectively (Berdie et al., 2017).

The TOPSIS methodology begins with the formulation of the normalise decision matrix r_{ij}, as shown in Eq. (2) represents how the auxetic scaffold design i satisfies the criterion j.

$$r_{ij} = \frac{x_{ij}}{\sqrt{\sum_{j=1}^{m} x_{ij}^2}}, j = 1, 2, \ldots, m, i = 1, 2, \ldots, n \tag{2}$$

where x_{ij} is the decision matrix of design candidate j evaluated for the criterion i. The matrix is subsequently normalised by multiplying the values with the criteria weights w_i as shown in Eq. (3):

$$\sum_{i=1}^{n} w_i = 1 \quad v_{ij} = w_i \times r_{ij}, j = 1, 2, \ldots, m, i = 1, 2, \ldots, n \tag{3}$$

For the decision-making scenario of the auxetic scaffolds presented in this study, a combined case of TOPSIS and 'analytical hierarchy process' (AHP) is required. While TOPSIS is used to identify the best design satisfying a range of parametric criteria, AHP allows specifying the relative weight for each of the criteria. AHP contributes to multi-objective decision-making where a hierarchy exists between the objective criteria used (Dohale et al., 2021). AHP helps construct a comparison of the objective criteria based on their relative importance on a scale of 1–9 commonly referend to as the Saaty scale (Vithalani and Vithalani, 2017) shown in Table 3.

The application of AHP starts with the formulation of a goal at the top level informed by a range of criteria at the second level and design candidates at the third level. The relative importance of the different criteria to satisfy the goal is then conceived using the Saaty rating. This is followed by a consistency check to evaluate the accuracy of the formulation followed by the creation of the relative parametric weights.

Subsequently, the negative and positive ideal solutions for the weighted normalised decision matrix are evaluated as shown in Eqs. (4) and (5) respectively:

$$A^* = \left\{v_1^*, v_2^*, \ldots, v_i^*\right\} = \left\{ \left(\underset{j}{Max} v_{ij} | i \in I' \right), \quad \left(\underset{j}{Min} v_{ij} | i \in I'' \right) \right\} \tag{4}$$

$$A^- = \left\{v_1^-, v_2^-, \ldots, v_i^-\right\} = \left\{ \left(\underset{j}{Min} v_{ij} | i \in I' \right), \quad \left(\underset{j}{Max} v_{ij} | i \in I'' \right) \right\} \tag{5}$$

where I' is associated with the benefit criteria, and I'' is associated with the cost criteria. The separation measures can then be calculated by using the n-dimensional Euclidean distance where the positive (D_j^*) and negative ideal solution (D_j^-) is given by Eqs. (6) and (7), respectively:

$$D_j^* = \sqrt{\sum_{i=1}^{n} \left(v_{ij} - v^*\right)^2}, j = 1, 2, \ldots, m \tag{6}$$

$$D_j^- = \sqrt{\sum_{i=1}^{n} \left(v_{ij} - v^-\right)^2}, j = 1, 2, \ldots, m \tag{7}$$

Once the distance to the ideal solution is calculated, the relative closeness to the ideal solution (CC_j^*), where the index value lies between 0 and 1 can be calculated using Eq. (8):

$$CC_j^* = \frac{D_j^-}{D_j^* + D_j^-}, j = 1, 2, \ldots, m \tag{8}$$

Lastly, the scaffold designs are ranked based on their relative proximity to the ideal solution according to the descending values of CC_j^* to identify the best design. The larger index value in the ranking matrix corresponds to the best-performing design (Yazdani and Payam, 2015). The TOPSIS approach can be used to make complex decisions, perform analysis, comparisons, and rankings of the identified alternative solutions. The classical TOPSIS technique addresses issues where all decision data are represented by numbers. Other several extensions have been suggested based on the initial TOPSIS technique, offering support for fuzzy or interval criteria, vagueness, lack of information, uncertainty, or fuzzy or interval weights to modelled imprecision (Roszkowska, 2011).

2.5.2. Scenarios for the selection of meta-biomaterial auxetic bone scaffolds

In porous materials, controlling Poisson's ratio can manipulate the strain stimulus during bone regeneration (Park and Kim, 2013). Previous studies (Park and Kim, 2013) have shown that the lateral elastic strain of the bone scaffolds during compression influences bone regeneration. Although a high negative lateral strain requires scaffolds with maximum $-\upsilon$, this can change as a result of patient-specific requirements. To demonstrate the selection of patient-specific meta-biomaterial scaffolds featuring different $-\upsilon$, the study conceived two cases namely Scenarios 1 (S1) and Scenarios 1 S2 considering five different parameters as listed in Table 4.

Scenario 1 (S1): Auxetic bone scaffold that offers near-zero $-\upsilon$

Meta-biomaterial bone scaffolds that offer a near-zero Poisson's ratio (ZPR) may be more suitable to emulate the behaviour of native tissues for certain injuries. In particular, minimising lateral strain at the implanted site while conveying axial compressive stresses may be beneficial for wound healing. Under such circumstances, meta-biomaterial architecture that offers a close to zero $-\upsilon$ can be beneficial and can offer a new direction in the development of patient-specific meta-biomaterial bone scaffolds. Soman et al. (2012) studied single- and double-layer Polyethylene glycol (PEG) auxetic scaffolds showing that ZPR would be beneficial in the engineering of cartilage, corneal and ligament tissues. Considering this recommendation, the first scenario of the scaffold selection looks at achieving a ZPR while maintaining the suitable porosity and mechanical performance requirement for load-bearing bone scaffolds in the order $-\upsilon > \varphi > \sigma_y > E > EoD$.

Scenario 2 (S2): Auxetic bone scaffold with highest $-\upsilon$

Mechanical stimulation is a critical factor that regulates bone regeneration and healing (Ngiam et al., 2010). Bone regeneration at a tissue-scaffold interface is influenced by the type and magnitude of the

Table 3
Saaty rating scale for analytical hierarchy process (AHP) (Berdie et al., 2017).

Rating	Meaning
1, 3, 5	Equal, moderate, strong
7, 9	Very strong, extreme
2, 4, 6, 8	Intermediate rating
1/3, 1/5, 1/7, 1/9	Equivalent rating for inverse comparison

Table 4
Summary of scenario-based decision-making criterion used for the selection of CoCrMo meta-biomaterial bone scaffold satisfying two different auxetic lateral strain criteria while satisfying the general requirements for load-bearing bone scaffolds.

Parameters of interest	Notation	Decision-making criteria	
		Scenario 1 (S1)	Scenario 2 (S2)
Poisson's ratio	$-\upsilon$	↓	↑
Porosity	φ	↑	
Normalised Yield strength	$\overline{\sigma_y}$	↑	
Normalised Elastic modulus	$\overline{E}$	↑	
Ease of design	EoD	↑	
Order of influence	-	$-\upsilon > \varphi > \sigma_y > E > EoD$	

mechanical stimulus. Although Kim et al. (2021) suggest that auxetic biomaterials with properties tailored to natural tissue offer an improved ability for tissue reconstruction, Velasco et al. (2015) found that bone tissue regeneration is influenced by the mechano-regulatory phenomenon where high micro-strains result in faster fibrous tissue regeneration. As such, bone scaffolds featuring high $-\upsilon$ may facilitate increased tissue reintegration due to the extended mechanical stimulus it offers (Perier-Metz et al., 2020; Milan et al., 2010). To this extent, the second scenario looks at identifying the best scaffold design that offers a high $-\upsilon$ while maintaining other relevant scaffolds parameters in the order $-\upsilon > \varphi > \sigma_y > E > EoD$.

3. Results and discussion

3.1. Suitability of Ashby's criterion for auxetic materials

The focus of the study is on developing a meta-biomaterial bone scaffold that exhibits auxetic behaviour suitable for on-demand additive manufacturing. The first step in this regard was to conceive suitable unit cells (UCs) that offer auxetic behaviour while featuring the necessary pore size for load-bearing bone scaffolds. As such, the selection of unit cell designs was informed by established auxetic concepts (Bertoldi et al., 2017; Zhang et al., 2018; Yang et al., 2019) that offer negative Poisson's ratio ($-\upsilon$). The Poisson's ratio of a traditional materials are positive (υ). When a material deviates from the norm and gives rise to a $-\upsilon$, such architectures are classified auxetic (Evans, 1991; Choi et al., 2019; Mirzaali et al., 2018, 2019; Wojciechowski, 2003). When auxetic architectures are conceived in biomaterials they form a class of materials referred to as meta-biomaterials.

Widely studied $-\upsilon$ materials are informed by either re-entrant (Spagnoli et al., 2015; Lekesiz et al., 2017; Alomarah et al., 2018; Jiang et al., 2019; Wang et al., 2018; Nečemer et al., 2019) or chiral (Jiang and Li, 2018; Han et al., 2019; Kolken and Zadpoor, 2017; Wojciechowski, 1987, 1989; Mizzi et al., 2015) unit cells. Although additive manufacturing is suitable for fabricating either of these auxetic material classes, the most studied variant is the re-entrant category. This is due to the simplicity of the re-entrant architecture make it suitable for a wide range of application. This study investigates five different UCs that may be suitable to be used as the foundation for auxetic meta-biomaterial bone scaffolds. Ashby's criterion was used to study the influence of porosity on the mechanical properties of the selected UCs at the design stage. According to Ashby (2006), cellular structures formed of repeatable UCs can be theoretically characterised using their relative density. Accordingly, the theoretical elastic modulus (E_{thr}) and compressive strength (σ_{thr}) of the cellular architecture can be related to their relative densities (ρ_r) using Eqs. (9) and (10), respectively:

$$E_{thr} \approx E\rho_r^{\,2} \tag{9}$$

$$\sigma_{thr} \approx \sigma_y \rho_r^{\left(\frac{3}{2}\right)} \tag{10}$$

where E and σ_y are Young's modulus and yield stress of the bulk material, as listed in Table 6. The density (ρ_{uc}) of the unit cell can be calculated as the ratio of their mass (m_{uc}) to volume (V_{uc}). Comparing the theoretical performance of the auxetic UCs informed by Ashby's criterion as shown in Fig. 5, UC1 offers the highest E_{thr} and σ_{thr} of 1.82 GPa (Fig. 5a) and 80.85 MPa (Fig. 5b), respectively informed by the lowest porosity. UC4 shows the lowest properties of 0.56 GPa (E_{thr}) and 33.53 MPa (σ_{thr}) due to the porosity. Overall, E_{thr} of all UCs falls below the elastic modulus of tibial cortical bone at 18 GPa (Hoffmeister et al., 2000; Rho et al., 1993; Zysset et al., 1999). This was expected due to the high porosity of the UC designs considered.

Ashby's criterion was also extended to predict the performance of the scaffold designs in relation to their relative density. This is done to evaluate the suitability of ρ_r to be used as an indicative tool to aid the design of meta-biomaterials. As expected, the performance of the scaffold designs closely followed their foundational UCs with AX1 and AX4 exhibiting the highest and lowest overall performance for both E_{thr} (Fig. 5a) and σ_{thr} (Fig. 5b). However, when the UCs were triaxially assembled to conceive the scaffolds, the relative density has been affected. The difference here seems to be primarily dependent on the shape of the unit cell.

Overall, the highest difference in ρ_r of 19.73% was observed when UC5 was assembled to conceive AX5 leading to improvements in both E_{thr} and σ_{thr}. This is primarily due to the unique shapes of UCs leading to a reduction of pore size when triaxially assembled to conceive the scaffold designs. For AX5 in particular the bell shape of the unit cells assembles itself into the void of the previous unit cell reducing the overall porosity. Similarly, the lowest difference in ρ_r of 1.27% was when UC3 was assembled to generate AX3; here the modified re-entrant architecture allows for minimal pore size intrusion during assembly preserving the overall ρ_r of the unit cell. Overall, it can be seen that when assembling auxetic unit cells to form scaffold designs, the difference in porosity can be up to $\sim$ 20%. Such differences are often not found in the case of regular unit cells as they do not feature significant angular struts necessitating unconventional strain behaviour. Despite the change in porosity, all scaffolds designed in this study offered a porosity above 80% that exceeds the requirement (>60%) for load-bearing bone scaffolds and as such can be considered potential candidates.

Although Ashby's criterion is a useful tool in to predict the mechanical properties of cellular structures, they do not take into consideration the shape of the unit cell. This is a critical criterion that requires careful consideration for this study due to the unconventional shapes of the unit cell leading to auxetic behaviour. As such, experimental tests on the fabricated scaffolds are carried out to characterise their mechanical performance.

Table 5
Physical parameters and porosity data of the L-PBF processed CoCrMo meta-biomaterial scaffolds.

Properties	L-PBF CoCrMo auxetic bone scaffolds				
	AX1	AX2	AX3	AX4	AX5
Mass (m) g	6.4	5.7	5.4	4.4	4.6
Relative density (ρ_r)	0.2695	0.2328	0.2183	0.1802	0.1884
Porosity (%)	73.05	76.72	78.17	81.98	81.16

Table 6
Material properties of laser-powder bed fused CoCrMo dense material obtained from tensile test data showing E, σ_y and σ_{ult} which are Young's modulus, yield strength and ultimate strength, respectively.

Identifier	E (GPa)	σ_y (MPa)	σ_{ult} (MPa)	Ref.
Tensile test	194.23 ± 1.63	975.6 ± 11	1169.81 ± 10.44	This study
Datasheet	200	1060	1200 ± 100	Mp et al. (2011)
Dolgov *et al.*	213	720	-	DolgovN et al. (2016)
Cornacchia *et al.*	200	550	975	(Cornacchia et al., 2100928)

3.2. Additive manufacturing

3.2.1. Powder characteristics

All the five bio-metamaterial auxetic scaffold designs are fabricated using CoCrMo superalloy feedstock featuring powder morphology as shown in Fig. 6. The feedstock particles are largely spherical with some smaller particles attached to larger ones to form satellite particles. Although not widespread, the occasional presence of elongated particles can also be observed from the SEM data. Overall, the particle size range

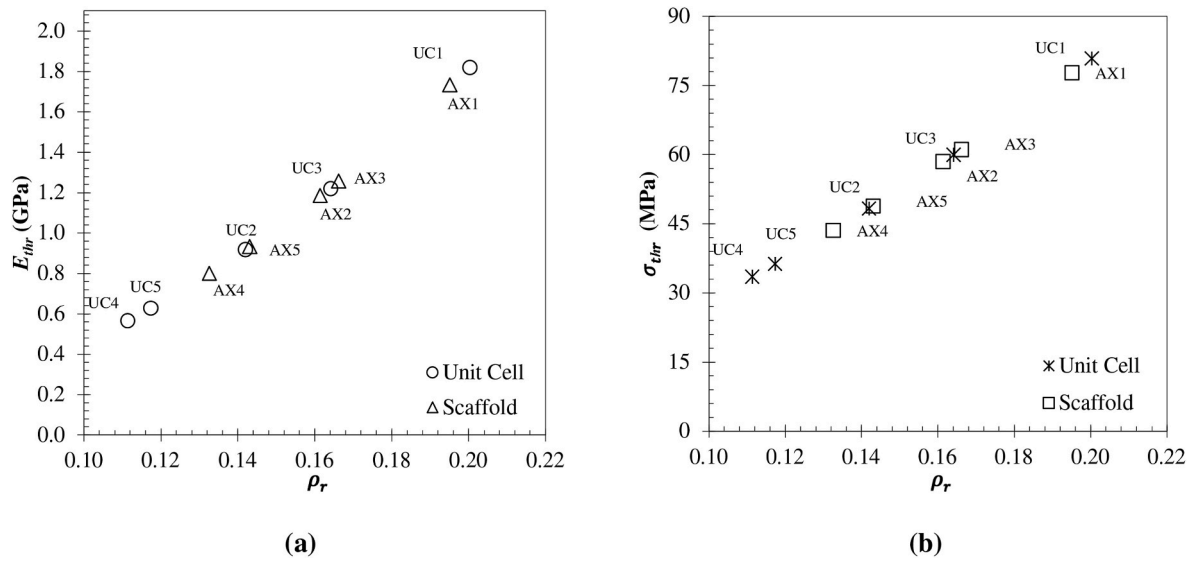

Fig. 5. The influence of relative density on the mechanical performance is informed by Ashby's criterion for the auxetic meta-biomaterial designs being conceived showing (a) the theoretical elastic modulus and (b) the yield strength for both the unit cells and the resulting scaffolds.

was measured to be between 5 and 85 μm. L-PBF benefits from a range of particle sizes as it influences both the flowability and the packing density at the powder bed leading to a dense melt track. The particle analysis found that the CoCrMo feedstock featured a volume and size distribution as shown in Fig. 7a and b, respectively. Particle analysis of the feedstock was carried out to characterise the mode, mean and median values of the volume fractions (D_{10}, D_{50}, and D_{90}) as shown in Fig. 7a. This data was subsequently used to identify excessively high or low particle distribution that can influence the L-PBF processability.

The particle volume distribution found a D_{10} of 13.2 μm, D_{50} of 28.8 μm and D_{90} of 46.1 μm indicating that at least 50% of the feedstock featured particles below 28.8 μm. A D_{10} and D_{90} of 13.2 and 46.1 μm indicate that the particle volume distribution is relatively even with only 10% of particles below 18.8 μm. The data shown in Fig. 7b can be used to explain this phenomenon where the smaller particles get attached to their larger counterparts forming satellite particles. When it comes to L-PBF, a D_{90} of 10 μm may deem the feedstock unsuitable (Pleass and Jothi, 2018); in comparison, the data from Fig. 7b confirms that the particle size distribution of the CoCrMo feedstock feature a near-normal size distribution that is optimum for L-PBF.

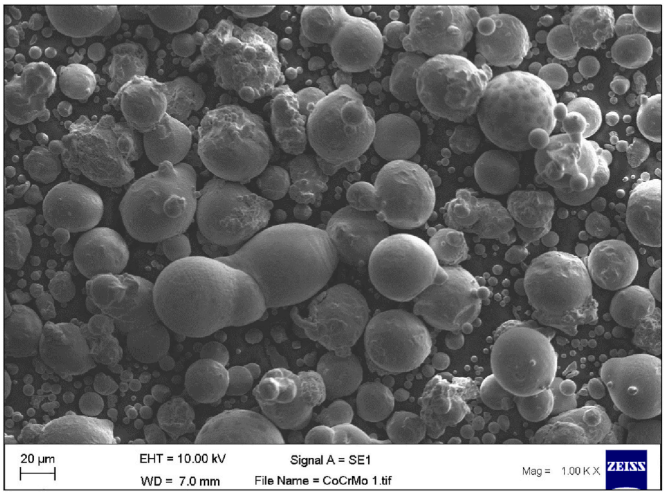

Fig. 6. Powder morphology of CoCrMo superalloy powder bed feedstock used for the laser powder bed fusion of the meta-biomaterial auxetic scaffolds.

3.2.2. Laser-powder bed fused meta-biomaterial scaffolds

L-PBF was used to additively manufacture the five meta-biomaterial scaffold designs (AX1-AX5) along with tensile test coupons, as shown in Fig. 8. As shown in Fig. 8a, the resulting scaffolds feature an open cellular architecture under varying strut orientation, pore size and porosity (Arjunan et al., 2020b). The varying pore size enhances vascularisation, resulting in increased bone ingrowth (Kang and Chang, 2018). While small pores are better for soft tissue growth, bigger pores often facilitate high permeability which is also beneficial for tissue-scaffold reintegration (Mohamed et al., 2019; Bordin et al., 2014). A 50–650 μm pore size and a porosity of more than 50% are required for efficient bone-scaffold ingrowth.

Three samples ($n = 3$) were built for each design (AX1-AX5) without using support structures owning to the sub-millimetre scale of the UCs offering relatively small overhang lengths. Post-printing, the test prototypes were separated from the base plate with the help of wire EDM. Shotblasting was used to remove the partially sintered and loose particles revealing a smoother surface (Fig. 8). The relative density of the scaffolds was then calculated as the ratio of the scaffold density to that of the bulk density. The density of the fabricated scaffolds was characterised as the ratio of experimental measured mass and volume by dry weighting and X-ray CT scan respectively.

The resulting porosity of the L-PBF scaffolds is as listed in Table 5 where a porosity range of 73%–82% was observed, which is slightly different to that of ideal CAD data at 80–87%. Although the L-PBF processed scaffolds resulted in a slightly lower porosity in comparison to their ideal counterparts, the overall trend in porosity distribution between the scaffolds was found to be similar (Fig. 9). The largest and smallest difference in porosity of 7.4% and 4.53% were observed for scaffolds AX1 and AX5 respectively. Overall, the average difference in porosity between CAD and actual scaffolds was 5.8%. To fully reveal the effect of L-PBF on the quality of the printed samples, an SEM-informed morphology analysis was carried out, the results of which are presented in the subsequent section.

3.2.3. Morphology of the printed meta-biomaterial scaffolds

SEM micrographs were used to evaluate the differences in porosity between ideal and printed scaffolds. Fig. 10 shows the influence of shot blasting on the printed samples. Comparing the struct quality before (Fig. 10a) and after (Fig. 10b), it is evident that the shot blasting removed most of the semi-molten and loose powdered particles from the scaffolds. However, on close inspection of joints, as shown in Fig. 10c,

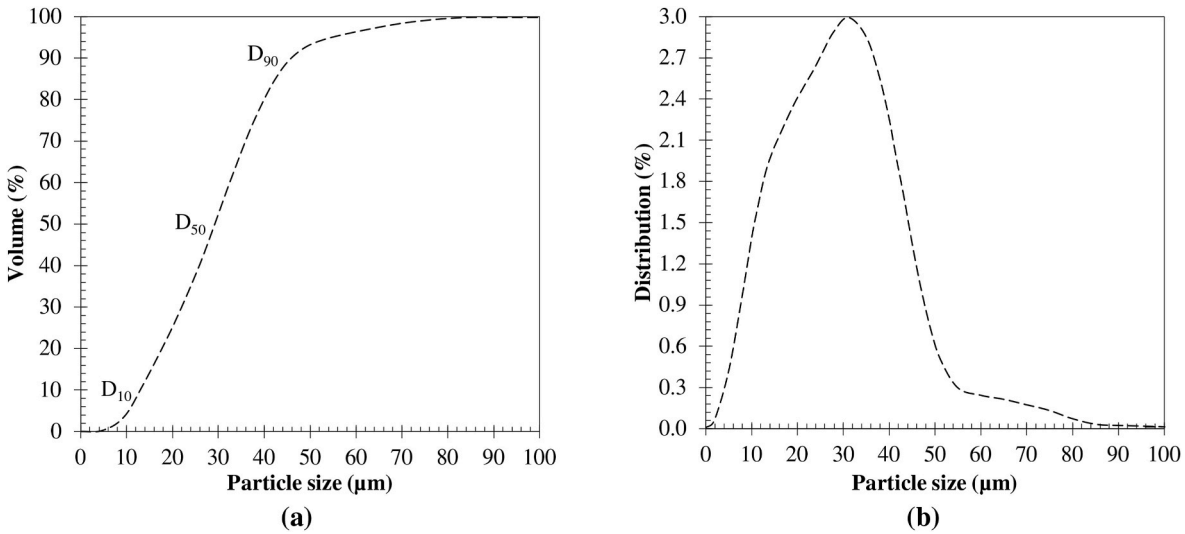

Fig. 7. Characteristics of the CoCrMo superalloy feedstock used for the laser powder bed fusion of meta-biomaterial scaffolds showing, (a) the particle volume distribution (PVD) and (b) the particle size distribution (PSD).

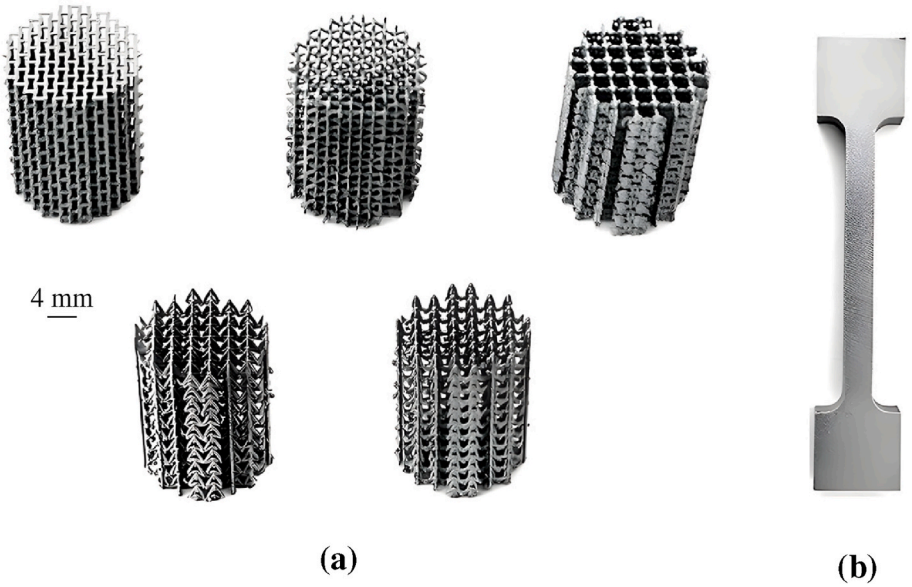

Fig. 8. Laser-powder bed fused CoCrMo superalloy meta-biomaterial showing (a) the fabricated auxetic bone scaffolds and (b) the tensile test coupons.

some semi-molten powders can be observed. Although this is at the micron scale, the large number of joints can contribute to a reduction in porosity which was also observed by Tan et al. (Bari and Arjunan, 2019).

A rough surface finish is also evident in both Figs. 10 and 11, which is representative of the additive manufacturing process. The SEM micrographs of all post-processed CoCrMo scaffolds are shown in Fig. 11. Although the data confirms open porosity closely mimicking the CAD data, the average variation in strut thickness was found to be ~ 50 μm. This observation is consistent with the literature (Ahmed et al., 2019; Zadpoor, 2017; Weiβmann et al., 2017; Tan et al., 2017) on L-PBF of thin walls below 300 μm. Overall, the dimensional variation of the L-PBF scaffolds showed a ~ 5.8% change in overall porosity. This means that the L-PBF meta-biomaterial scaffolds show a 5.8% lower average porosity in comparison to their ideal counterparts.

Comparing the variations in strut thickness observed here with that of literature, Benedetti et al. (2019) reported that the struts parallel to the building direction have an oversizing tendency largely driven by the laser beam size in comparison to the strut thickness being printed. Furthermore, the existence of un-melted particles bound to the struts can also be a cause of disparity in strut dimension. Although similar observations were found in other studies (Hazlehurst, 2014; Bari and Arjunan, 2019), the uneven surface finish in interconnected porosity was highlighted as favourable for tissue ingrowth. In summary, the observations in Fig. 11 are consistent with literature with strut thickness deviating from the original design without largely affecting porosity. It can be seen that there is both over and under-sizing of the strut thickness due to the L-PBF process. However, the variation in strut thickness was largely influenced by strut orientation, with vertically oriented struts under-sized and horizontally oriented struts over-sized (Echeta et al., 2020).

3.3. Mechanical properties of L-PBF CoCrMo

Mechanical tests were conducted on dense CoCrMo tensile test coupons manufactured using L-PBF process parameters identical to that used for scaffold fabrication. Altogether three tensile test coupons (n =

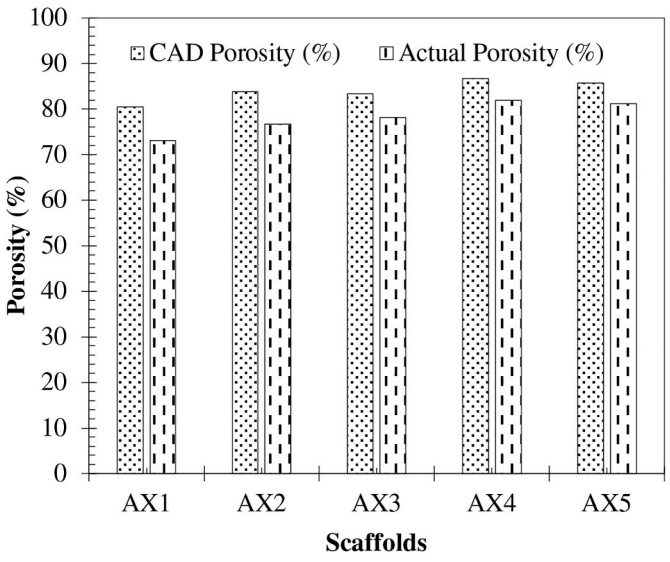

Fig. 9. Comparison of porosity between ideal and actual scaffolds.

3) were axially pulled under quasi-static test conditions to characterise the mechanical properties of L-PBD bulk CoCrMo superalloy. The resulting stress-strain ($\sigma - \varepsilon$) curve (Fig. 12a) along with the failed tensile samples (Fig. 12b). Fig. 12a shows consistent linear and non-linear for all the three test coupons that were pulled. Although identical L-PBF process parameters were used to print all the test coupons, a standard deviation of ±1.63 GPa, ±11 MPa and ±10.44 MPa was observed for E, σ_y and σ_{ult} respectively as summarised in Table 6. Comparing the mechanical performance results as revealed in Table 6, it can be seen the parameters describing the strength (σ_y and σ_{ult}) of the material closely follow the material properties datasheet (Mp et al., 2011).

Overall, a 2.54% and 8.29% difference was observed for σ_{ult} and σ_y, respectively between in-house test and the EOS datasheet (Mp et al., 2011). When it comes to Young's modulus, a ~ 3% difference was found in comparison to the datasheet and Dolgov et al. (DolgovN et al., 2016). This was expected due to the process parameters and heat treatment regimens used for the low stiffness variant of CoCrMo superalloy which is more suitable for biomedical applications. To put these observations into perspective, the cumulative parameter, 'laser energy density (e_{ld})' is introduced (Yakout et al., 2019; Maamoun et al., 2018; Ciurana et al., 2013; Read et al., 2015) as shown in Eq. (11):

$$e_{ld} = \frac{P_l}{v_s \times h_s \times t_l} \tag{11}$$

where e_{ld} (J/mm^3), P_l (W), t_l (mm), v_s (mm/s) and h_s (mm) represents the energy density, laser power, layer thickness, scan speed and hatch distance, respectively (de Terris et al., 2019; Li et al., 2019).

When it comes to L-PBF, the process parameters that constitute e_{ld} influences the thermo-physical behaviour during laser processing

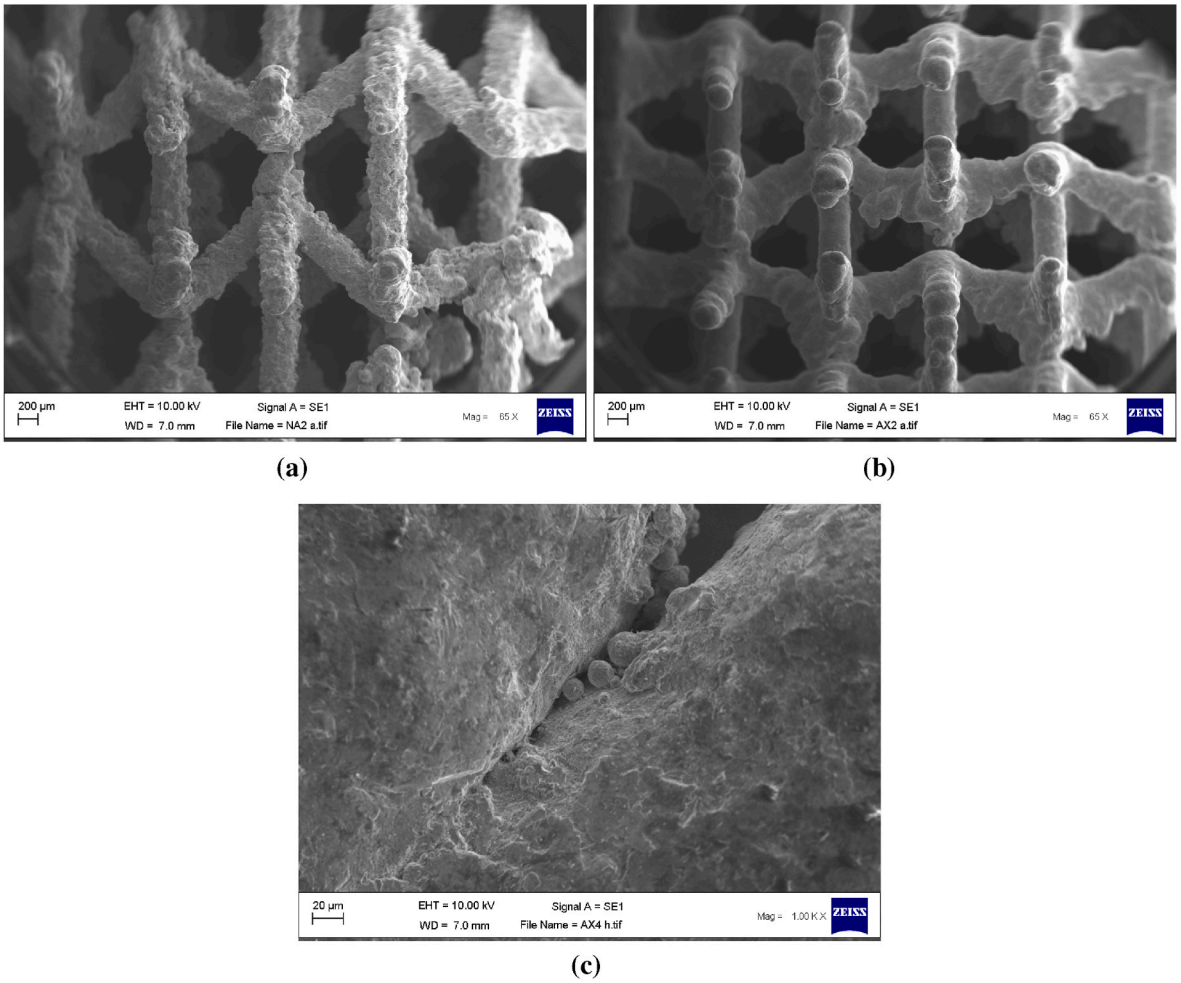

Fig. 10. Scanning electron microscopy data showing (a) scaffold as manufactured before shot blasting, (b) after shot blasting and (c) surface quality and powder adherence at joints post shot blasting.

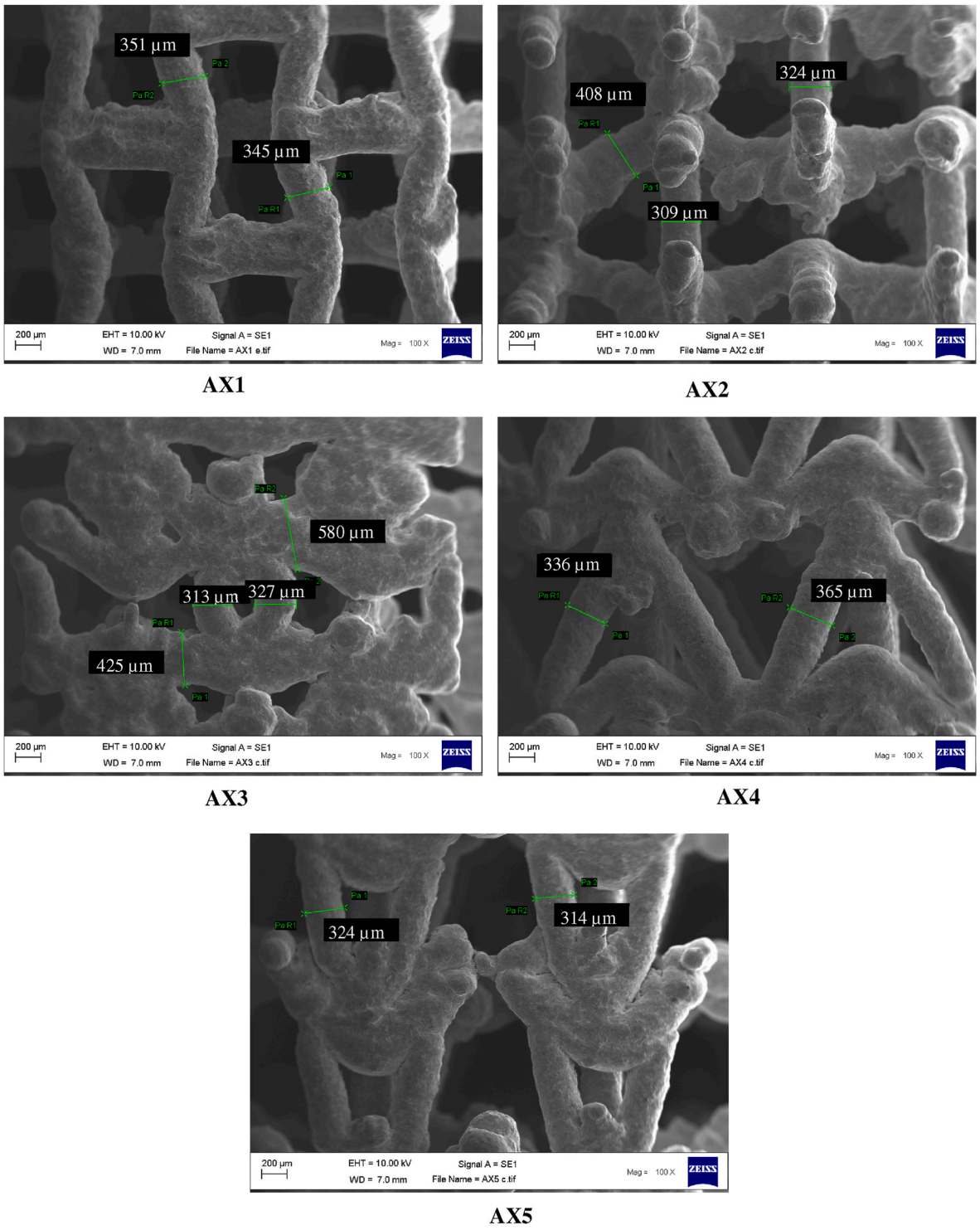

Fig. 11. Scanning electron micrography data showing the influence of laser-powder bed fusion on strut dimension of the different meta-biomaterial CoCrMo auxetic scaffolds namely AX1, AX2, AX3, AX4 and AX5.

influencing the mechanical properties of the fused material. In addition, the L-PBF processed samples were heat-treated at 1150 °C for 6 h which often helps to reduce the elastic modulus of the material improving its suitability for biomedical applications. The methodology for this is further explained in the context of other L-PBF materials in studies by Arjunan et al. (2020e). Lowering, the E value of the bulk material is critical to reducing the stress shielding and maladapted stress concentration at the scaffolds implant interface when it comes to load-bearing applications. Overall, the mechanical performance closely follows both the material test data and other literature in the area of laser-powder bed processing.

3.4. Elastic-plastic performance of CoCrMo auxetic scaffolds

The compressive $\sigma - \varepsilon$ curve of the L-PBF processed CoCrMo auxetic bone scaffolds are summarised in Fig. 13. Overall, all the curves show two distinctive regions describing both the elastic and plastic behaviour of the different meta-cellular architectures. In all curves, the initial

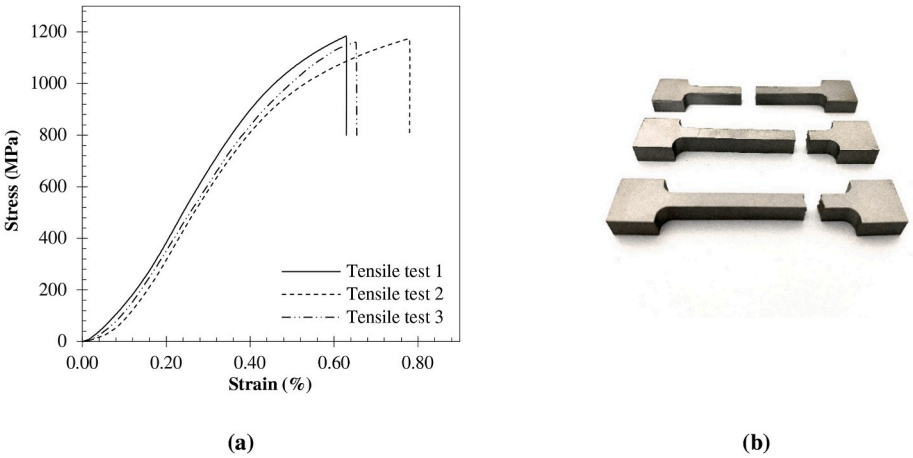

Fig. 12. Mechanical performance of laser-powder bed fused CoCrMo superalloy dense material showing (a) the stress-strain relationship and (b) the failed tensile test coupons.

region of the curve reveals the linear performance, immediately followed by the non-linear elastic performance ending at σ_{ult} (Mahbod and Asgari, 2019). The subsequent reduction in stress indicates the beginning of the plateau region. This region is signified by stress fluctuations or serrations as shown in Fig. 13 (Pham et al., 2012). The plateau region continues until all the cell walls collapse and the material starts to densify reducing the overall porosity.

Looking at the stress-strain performance of each of the auxetic scaffolds being tested as shown in Fig. 13a–e. AX1 (Fig. 13a) showed the highest σ_y and E of 56 MPa and 1.66 GPa, respectively between all the meta-biomaterial architectures tested. The reason for this high performance is evident from the $\sigma - \varepsilon$ curve where lower stress at plateau collapse can be observed. This is due to the re-entrant architecture distributing the strain across the cellular architecture significantly reducing the possibility of localised failure.

On the contrary, AX2 showed a localised collapse at 4.6% of the strain before steadily climbing to peak stress of around 90 MPa before the wall collapse occurs as shown in Fig. 13b. The performance indicates an initial localised failure by the structure without involving the subsequent cellular layers during the initial part of the compression. This effect is a result of the distinctive vertical beams in UC2 that resist most of the axial load. The vertical beams above the top surface act as isolated load-bearing elements resulting in localised failure before engaging the meta-biomaterial architecture. However, as soon as the vertical beams fail, the cross walls interact with the structure stabilising the architecture and allowing it to withstand a higher load. Due to this unique phenomenon, AX2 showed the lowest yield strength of 32 MPa amongst all the meta-biomaterial architectures tested as summarised in Table 7.

At an E and σ_y of 1.57 GPa and 36 MPa, AX3 underperformed AX1 by 5.5% and 43.5%, respectively. The comparatively large reduction in σ_y is due to $-\upsilon$ of AX3 being close to zero (−0.1). This means that the compression is accommodated by the cell walls moving vertically down with minimal lateral movement leading to catastrophic failure of the cell walls signified by the large reduction in σ_y (Fig. 13c). The post-yield plastic behaviour of AX3 also shows a lower capacity to resist the stress being developed, signified by low plastic peaks. The catastrophic failure of the AX3 architecture can be observed in Fig. 14c, confirming these observations.

AX4 and AX5 have similar $-\upsilon$ of −0.16 and show $\sigma - \varepsilon$ performance comparable to that of cellular materials that show initial localised failure and post-yield behaviour signified by progressive failure of cellular layers. Some peeling of boundary cells can also be observed for AX5, causing an initial large drop and subsequent high peak in plastic stresses. For the biomedical application of auxetic structures, the stiffness, strength and Poisson's ratio are the key parameters informing the meta-biomaterial scaffold design (Soro et al., 2019; Singh et al., 2010; Hendrikson et al., 2017). Comparing the mechanical performance of all the five meta-biomaterial scaffolds, as summarised in Table 7, AX1 offers the highest elastic modulus, yield strength and negative Poisson's ratio.

Overall, all architectures showed varying degrees of auxetic behaviour signified by the range of negative Poisson's ratios as shown in Table 7. Comparing the performances of the scaffolds, the elastic modulus of the structures varied by 1.13–1.66 GPa, and the yield strength by 32–56 MPa, with AX2 underperforming all the other scaffolds. Previous compressive test studies on non-auxetic cellular materials showed that the elastic modulus and strength of these materials are strongly influenced by their unit cell shape; a trend that was also observed in this study (Hazlehurst, 2014). Nevertheless, compressive test results showed that there is no significant trend between elastic modulus and the yield strength among auxetic materials.

3.5. Meta-cellular failure modes

The morphology of individual cells along with their neighbouring connections in a meta-biomaterial architecture influences the structural performance of the scaffold. In this regard, studying the global deformation of the auxetic scaffolds can reveal the influence of pore shape on the failure modes. Fig. 14 shows selected still frames during quasi-static compression to characterise the plastic deformation and failure of the meta-biomaterial architecture. The chosen slides from the recorded image being presented represent the initial uncompressed scaffold; the moment of the initial failure followed by 10%, 20% and 30% post-yield compression.

Despite all porous architectures being auxetic, the differences in unit cell shape can be seen to influence both the compressive behaviour and failure modes of the scaffolds (Fig. 14). The 10% compression of all the scaffolds (Fig. 14a-e) demonstrates an inward lateral strain under compression, confirming the negative Poisson's ratio. The uniform contraction of the structure demonstrates that the pore geometry significantly impacts the deformation behaviour. The deformation of AX2 and AX4 as shown in Fig. 14b and d respectively shows comparatively low elastic modulus informed by their unit cell geometries. The similarity in performance can be due to both meta-biomaterial architectures being based on the arrowhead design albeit featuring different parametric values.

AX1 shows uniform shrinkage up to 10% axial compression, followed by localised failure initiated at the top cellular layer as shown in Fig. 14a. While AX5 also showed failure initiating at the top, the peeling of boundary beams resulted in a large drop in stress post-yield. On the contrary, AX3 did not show crush bands; instead failed catastrophically

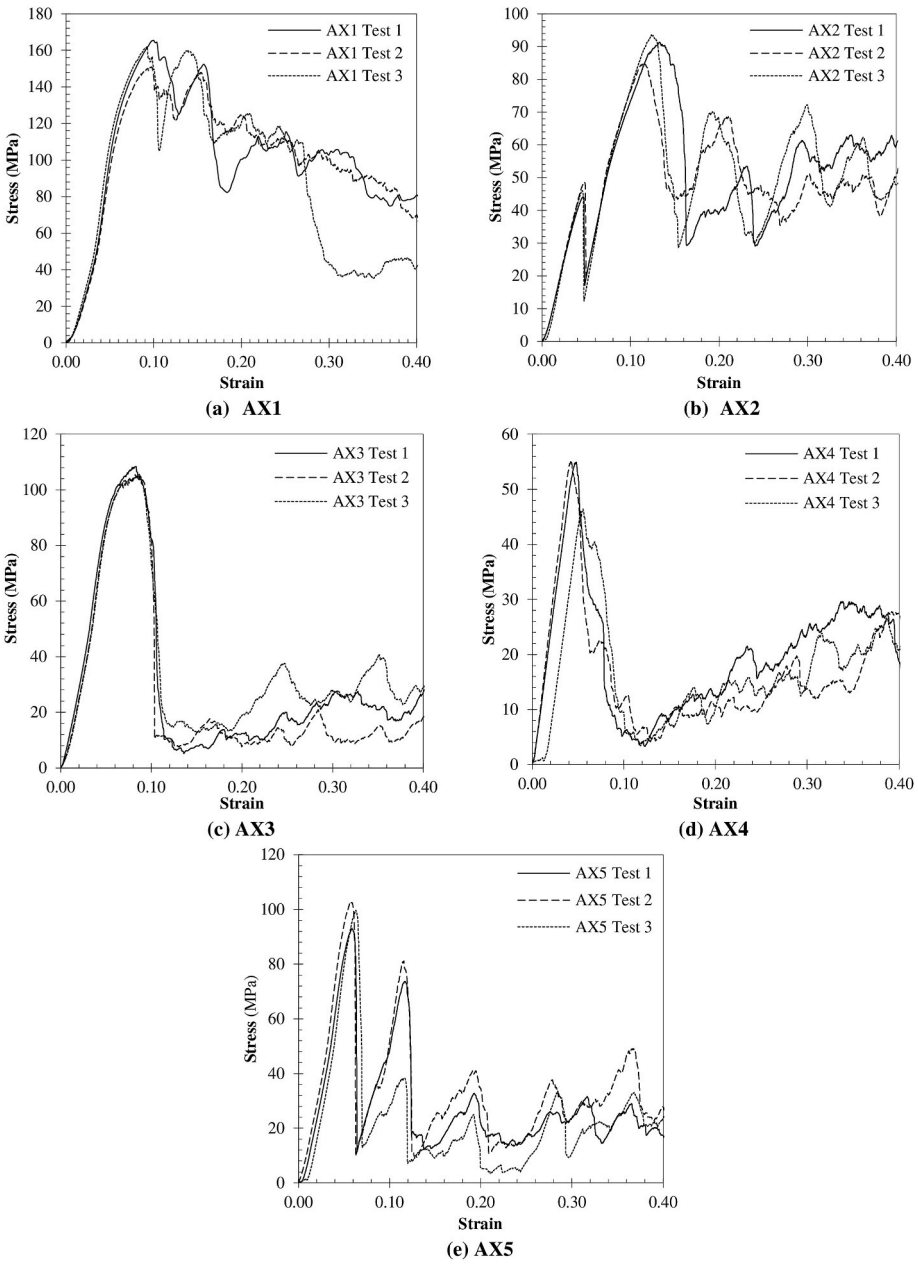

Fig. 13. The stress-strain relationship for L-PBF CoCrMo auxetic bone scaffolds is informed by physical tests showing the different meta-biomaterial architectures (a) AX1, (b) AX2, (c) AX3, (d) AX4 and (e) AX5.

Table 7
Mechanical behaviour of L-PBF processed CoCrMo auxetic meta-biomaterial bone scaffolds informed by physical experimental test data where φ, E, σ_y, σ_{ult} and $-\upsilon$ are the porosity, elastic modulus, yield strength, ultimate strength, and the negative Poisson's ratio, respectively.

Scaffold	φ (%)	E (GPa)	0.2% σ_y (MPa)	σ_{ult} (MPa)	$-\upsilon$
AX1	73.05	1.66 ± 0.47	56 ± 1.24	158.0 ± 6.65	−0.24
AX2	76.72	1.13 ± 0.02	32 ± 0.81	88.87 ± 3.49	−0.13
AX3	78.17	1.57 ± 0.02	36 ± 0.62	104.53 ± 2.40	−0.10
AX4	81.98	1.27 ± 0.03	52 ± 4.71	51.66 ± 4.14	−0.16
AX5	81.16	1.60 ± 0.08	40 ± 0.84	97.90 ± 3.83	−0.16

as a result of crack propagation as shown in Fig. 14c. This is a result of the low lateral strain signified by $-\upsilon$ close to zero.

SEM data of the scaffolds are extracted as shown in Fig. 15 to further characterise the deformation modes of the meta-biomaterial architecture.

For additively manufactured cellular materials with beam thickness close to 300 μm, the micro-scale inconsistencies as a result of the L-PBF process are often highlighted as yield initiators (Ahmed et al., 2019; Genovese et al., 2017; Dong et al., 2018). The reason for this is the micro-scale inconsistencies acting as stress raisers as observed by Yu et al. (2019). In comparison, Fig. 15a to e shows that the failure of the meta-biomaterial is primarily informed by the cellular architecture and the quality of inter-cellular joints rather than L-PBF induced micro-scale variations in beam thicknesses. In particular, AX1 shows a tensile failure of the crossbeam as shown in Fig. 15a indicating that the failure is initiated by the re-entrant beam that stretches laterally to accommodate the negative strain. When it comes to AX2 and AX3, the failure seems to be initiated at the joints, as shown in Fig. 15b and c which also explains the comparatively low yield strength observed for these architectures. This kind of deformation is often the result of progressive folding of the beams at the joints or the stress concentration. The abrupt change in

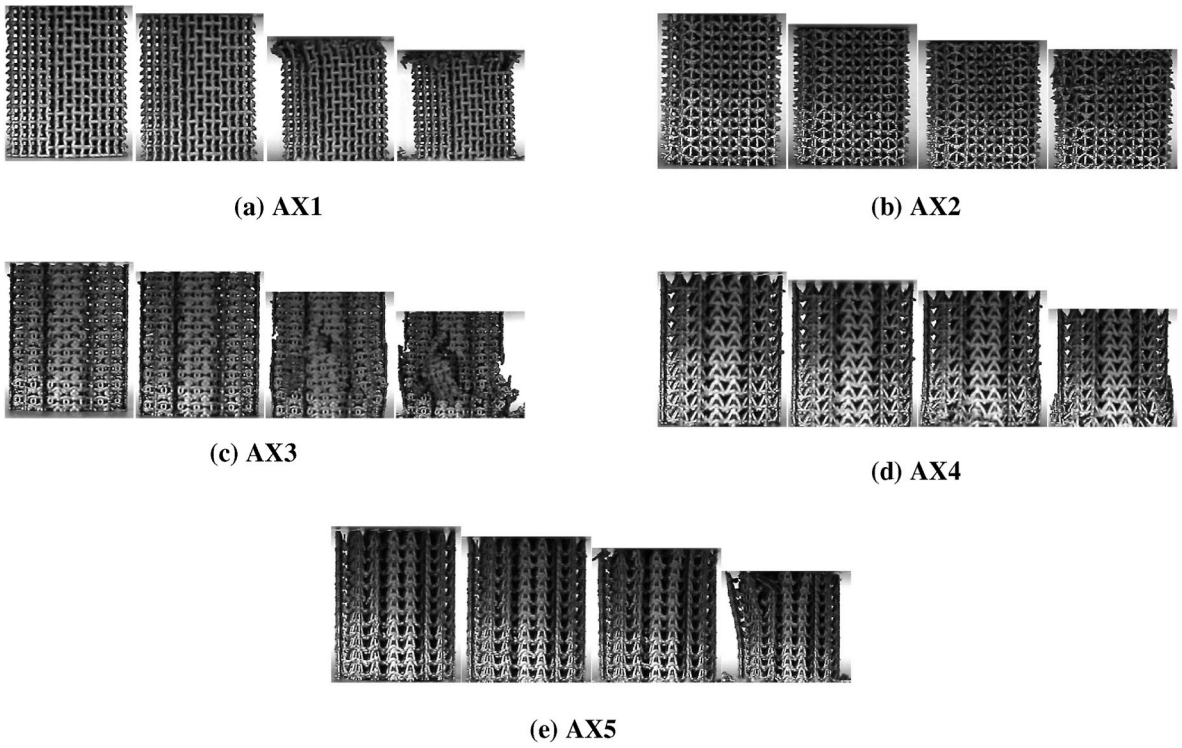

Fig. 14. Deformation of the CoCrMo auxetic scaffolds showing 0%, 10%, 20% and 30% deformation of the meta-biomaterial architectures (a) AX1, (b) AX2, (c) AX3, (d) AX4 and (e) AX5.

geometry of AX2 indicates significant stress concentration, which can be a contributing factor.

A bending-induced failure can be observed for AX4 and AX5 as shown in Fig. 15d and e respectively indicating progressive folding during compression facilitated by the arrowhead and bell shape unit cells. Overall, none of the meta-biomaterial architecture shows thinning of the beams (Fig. 15), evidencing a brittle behaviour that is generally observed for L-PBF processed cellular metals (Dong et al., 2018; Kan et al., 2019; Hadadzadeh et al., 2019). Nevertheless, the majority of the failure modes for the meta-biomaterials seem to be dictated by unit cell collapse, which is different to traditional cellular materials where distinctive shear plane cutting across multiple cellular layers are often observed (Chen et al., 2019; Yan et al., 2014; Liu et al., 2019).

3.6. Multi-criteria decision making

The multi-criteria decision-making technique used in this study combines the AHP and TOPSIS methodologies for case-based identification of the best-performing meta-biomaterial architecture. AHP scores and set the share of relative importance for the choice criteria sets. Alternatives in the hierarchy are the five (AX1 to AX5) scaffold designs influenced by five decision-making criteria namely, the Poisson's ratio (υ), Porosity (φ), yield strength (σ_y), elastic modulus (E) and ease of design (EoD). All responses used for the decision-making matrix were experimentally evaluated as summarised in Table 8 with EoD being a subjective criterion. As such EoD ranking depends on both the software and the expertise of the user designing the unit cells. The TOPSIS approach is used to rank a relatively weighted matrix from best to worst performing meta-biomaterial architecture considering all the five objective parameters.

To offer a like-for-like comparison, the yield strength and elastic modulus are normalised with respect to relative density neutralising the differences in porosity. The ease of design parameter is conceived from a five-point numerical scale, where 5 and 1 are the simplest and most complex designs, respectively. All the data used for the decision support model is summarised in Table 8. The decision-making and weighting criteria are developed based on the two specific selection criteria (Scenario 1 and Scenario 2) as presented in subsequent sections. For all cases, the parametric importance of the criteria is of the form $\upsilon > \varphi > \sigma_y > E > EoD$.

3.6.1. Scenario 1: Auxetic bone scaffold with near-zero $-\upsilon$

In the analytic hierarchy process, the importance values decide the criteria weights. Since the nature of the meta-biomaterial presented in this study is auxetic, Poisson's ratio has the highest importance of all the alternatives. To identify the best meta-biomaterial architecture that satisfies scenario one, the lowest value of the $-\upsilon$ is set as the ideal. To facilitate this in the pair-wise matrix, inverse values are used for $-\upsilon$ row, as shown in Table 9.

The pair-wise matrix is normalised by dividing all the values in Table 9 by the sum of the column resulting in the normalised pairwise comparison matrix shown in Table 10. Finally, the relative weights of each criterion for the selection of the ideal design are calculated by averaging all the element values in each row (Table 10), resulting in Table 11.

The TOPSIS approach is used in the final stage to fulfil the desired objectives. The main principle of this process is that the best alternative (AX1 to AX5) lies close to the ideal alternative. In this regard, the best design is identified as rank one, while the worst option is zero (Berdie et al., 2017). The normalised values related to the criteria shown in Table 12 were calculated from the decisional matrix in Table 8 by using Eq. (2). The normalised weighted matrix, as shown in Table 13, was calculated using Eq. (3) by multiplying each element of each column of Table 12 by the relative criteria weights as identified in Table 11. Subsequently, the negative and positive ideal solutions, as listed in Table 14, were calculated for the weighted normalised decision matrix (Table 13) by using Eqs. (4) and (5).

Once A^* and A^- are obtained as shown in Table 14, the separation distance of each competitive alternative from the positive (D_j^*) and negative (D_j^-) ideal solutions were calculated using Eqs. (6) and (7). In

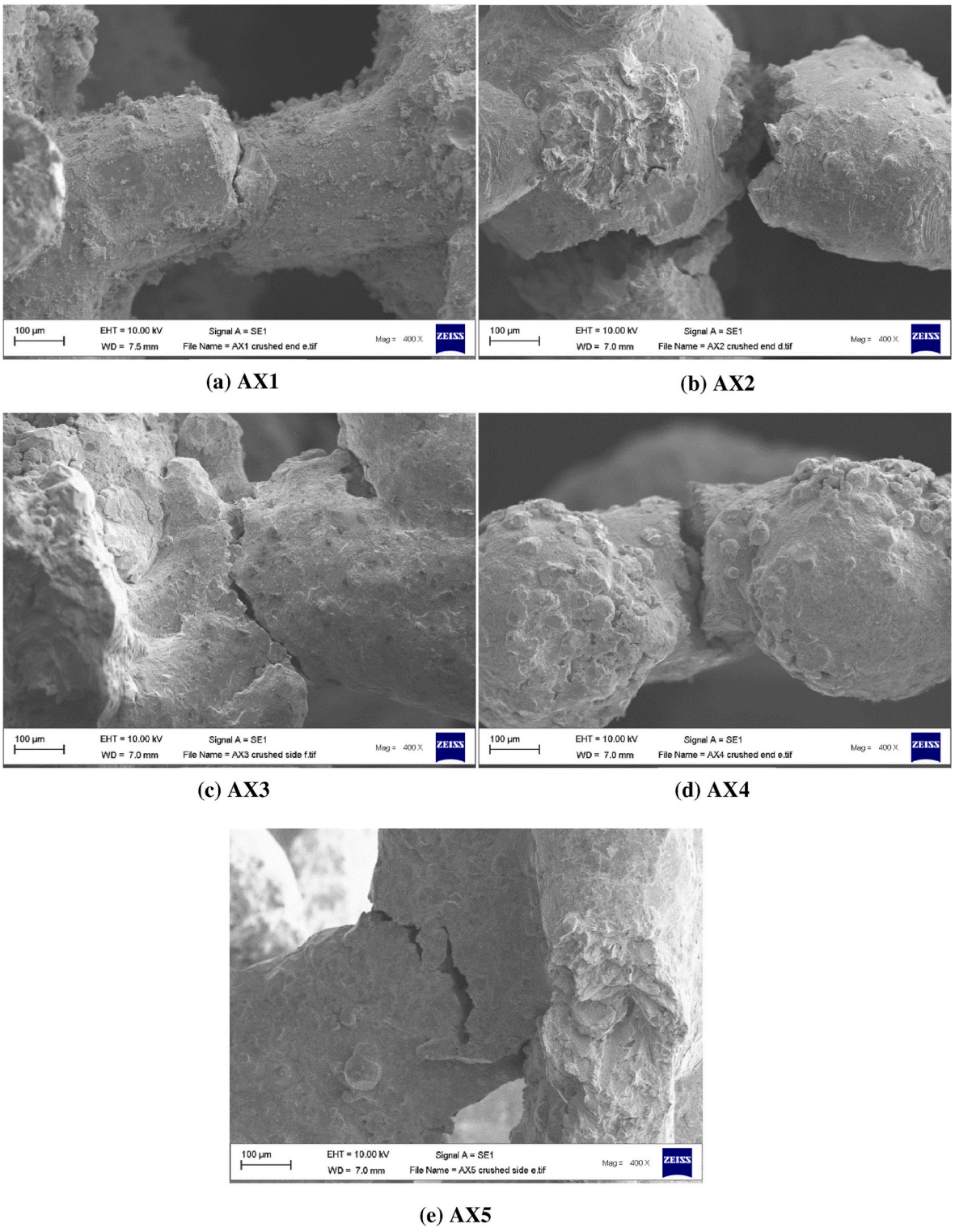

Fig. 15. SEM data of the failed CoCrMo auxetic bone scaffold highlighting failure regions to inform the failure mode analysis for (a) AX1, (b) AX2, (d) AX3, (d) AX4 and (e) AX5.

addition, the relative closeness value was calculated using Eq. (8). Finally, the scaffold alternatives were ranked based on the closeness values to identify the best design, as shown in Table 15. It can be seen that the combined AHP and TOPSIS method identified AX4 to be the best scaffold design to offer a near-zero Poisson's ratio (Scenario 1) while meeting all the other objective criteria set for scenario 1. The procedure is repeated to identify the best design for another set of objective parameters classified as Scenario 2 which is explained in the subsequent section.

3.6.2. *Scenario 2: Auxetic bone scaffold with highest* $-\upsilon$

For scenario two, identifying a scaffold with the highest $-\upsilon$ while maintaining good performance to other relevant parameters as summarised in Table 4 is required. Table 16 shows the AHP pairwise

Table 8
Decisional matrix and the parametric values used for multi-criteria decision making.

Design	υ	φ (%)	σ_y (*MPa*)	E (*GPa*)	*EoD*
AX1	−0.24	73.05	207.78	6.16	4
AX2	−0.13	76.72	137.47	4.85	1
AX3	−0.10	78.17	164.90	7.19	2
AX4	−0.16	81.98	288.50	7.05	5
AX5	−0.16	81.16	212.28	8.49	3

Table 9
Pair-wise comparison matrix to determine the relative importance of the five parameters contributing to the selection of a near-zero Poisson's ratio auxetic bone scaffold.

Parameters	υ	φ	σ_y	E	*EoD*
υ	1	1/3	1/5	1/7	1/9
φ	3	1	3	5	7
σ_y	5	1/3	1	3	5
E	7	1/5	1/3	1	3
EoD	9	1/7	1/5	1/3	1
Sum	25	2.01	4.73	9.48	16.11

Table 10
Normalised pair-wise comparison matrix to determine the relative importance of the selected parameters.

Parameters	υ	φ	σ_y	E	*EoD*
υ	0.0400	0.1659	0.0423	0.0151	0.0069
φ	0.1200	0.4976	0.6338	0.5276	0.4345
σ_y	0.2000	0.1659	0.2113	0.3166	0.3103
E	0.2800	0.0995	0.0704	0.1055	0.1862
EoD	0.3600	0.0711	0.0423	0.0352	0.0621

Table 11
Criteria relative weights show the importance of the selected parameters in the selection of a near-zero Poisson's ratio auxetic bone scaffold.

Criteria	Criteria weight
Poisson's ratio	0.0540
Porosity	0.4427
Yield strength	0.2408
Elastic modulus	0.1483
Ease of Design	0.1141

Table 12
The normalised values are related to the criteria.

Design	υ	φ	σ_y	E	*EoD*
AX1	0.6515	0.4173	0.4455	0.4018	0.5394
AX2	0.3529	0.4383	0.2947	0.3167	0.1348
AX3	0.2715	0.4466	0.3535	0.4692	0.2697
AX4	0.4343	0.4683	0.6185	0.4597	0.6742
AX5	0.4343	0.4636	0.4551	0.5539	0.4045

Table 13
Weighted normalised matrix for scenario 1.

Design	υ	φ	σ_y	E	*EoD*
AX1	0.0352	0.1848	0.1073	0.0596	0.0616
AX2	0.0191	0.1940	0.0710	0.0470	0.0154
AX3	0.0147	0.1977	0.0851	0.0696	0.0308
AX4	0.0235	0.2073	0.1490	0.0682	0.0769
AX5	0.0235	0.2053	0.1096	0.0822	0.0462

Table 14
Positive and negative ideal solutions for scenario 1.

Parameters	υ	φ	σ_y	E	*EoD*
Positive Solution (A^*)	0.0147	0.2073	0.1490	0.0822	0.0769
Negative Solution (A^-)	0.0352	0.1848	0.0710	0.0470	0.0154

Table 15
Ranking matrix identifying the best auxetic scaffolds meeting all the decision criteria while offering a near-zero Poisson's ratio satisfying scenario 1.

Design	(D_j^*)	(D_j^-)	Relative closeness (CC_j^*)	Rank
AX1	0.0584	0.0601	0.507	3
AX2	0.1063	0.0186	0.149	5
AX3	0.0803	0.0392	0.328	4
AX4	0.0165	0.1047	0.864	1
AX5	0.0508	0.0651	0.562	2

comparison matrix informed by the Saaty scale (Table 3) showing the relative importance of the parameters. The resulting normalised pair-wise comparison matrix (Table 17) is obtained by dividing the elements of the column by the sum of the column in Table 16. Finally, the criteria weights from the AHP process are calculated by averaging all the element values in each row resulting in Table 18.

Once the criteria of relative weights have been assigned to all the five objective criteria (Table 18), the TOPSIS method is used to identify the best meta-biomaterial scaffold satisfying Scenario 2. The scaffold design which receives CC_j^* closer to 1 is the best candidate based on the decision-making criteria used. The normalised values related to the criteria in Table 12 were used for Scenario 2 with criteria weights listed in Table 18. Table 19 shows the normalised weighted matrix shown calculated using Eq. (3) by multiplying each element of each column of the normalised decision matrix (Table 12) by the relative criteria weights (Table 18).

Subsequently, the negative and positive ideal solutions, as shown in Table 20, were evaluated for the weighted normalised decision matrix by using Eqs. (4) and (5). The separation distance for each scaffold designs from the positive (D_j^*) and negative (D_j^-) ideal solutions were calculated using Eqs. (6) and (7). In addition, Eq. (8) was used to calculate the relative closeness values resulting in the ranking as shown in Table 21. The results of the combined AHP and TOPSIS method identified that the most suitable auxetic scaffold design for Scenario 2 is AX1.

4. Limitations and challenges

For meta-biomaterials to be commonplace in tissue reconstruction, multiple limitations require addressing. When it comes to additive manufacturing, structural integrity at the sub-micron scales suitable for the fabrication of meta-biomaterials remains a primary limitation. Furthermore, improvements in reducing contamination during fabrication and post-processing are also necessary. While the latest L-PBF technique meets the basic requirements for the fabrication of meta-biomaterials, there is still a need for achieving smaller dimensions, improved dimensional accuracy, and consistent mechanical properties

Table 16
AHP pair-wise comparison matrix for scenario 2.

Design	υ	φ	σ_y	E	*EoD*
υ	1	3	5	7	9
φ	1/3	1	3	5	7
σ_y	1/5	1/3	1	3	5
E	1/7	1/5	1/3	1	3
EoD	1/9	1/7	1/5	1/3	1
Sum	1.79	4.68	9.53	16.33	25

Table 17
Normalised pair-wise comparison matrix for scenario 2.

Design	υ	φ	σ_y	E	EoD
υ	0.5595	0.6415	0.5245	0.4286	0.3600
φ	0.1865	0.2138	0.3147	0.3061	0.2800
σ_y	0.1119	0.0713	0.1049	0.1837	0.2000
E	0.0799	0.0428	0.0350	0.0612	0.1200
EoD	0.0622	0.0305	0.0210	0.0204	0.0400

Table 18
Criteria of relative weights for scenario 2.

Criteria	Criteria weight
Poisson's ratio	0.5028
Porosity	0.2602
Yield strength	0.1344
Elastic modulus	0.0678
Ease of Design	0.0348

Table 19
Weighted normalised matrix.

Design	υ	φ	σ_y	E	EoD
AX1	0.3276	0.1086	0.0598	0.0272	0.0188
AX2	0.1774	0.1141	0.0396	0.0215	0.0047
AX3	0.1365	0.1162	0.0475	0.0318	0.0094
AX4	0.2184	0.1219	0.0831	0.0312	0.0235
AX5	0.2184	0.1207	0.0611	0.0375	0.0141

Table 20
Positive and negative ideal solutions for scenario 2.

Parameters	υ	φ	σ_y	E	EoD
Positive Solution (A^*)	0.3276	0.1219	0.0831	0.0375	0.0235
Negative Solution (A^-)	0.1365	0.1086	0.0396	0.0215	0.0047

Table 21
Ranking of alternatives for Scenario 2.

Design	(D_j^*)	(D_j^-)	Relative closeness (CC_j^*)	Rank
AX1	0.0291	0.1928	0.869	1
AX2	0.1585	0.0413	0.207	4
AX3	0.1951	0.0158	0.075	5
AX4	0.1094	0.0960	0.468	2
AX5	0.1118	0.0875	0.439	3

to streamline the integration of AM meta-biomaterials into a clinical setting. In addition to manufacturing, there are also design-related challenges: For example, the limited research into this area means that it is often not clear what exact geometries would give rise to the most desired properties for a given scenario. Given that stiffness matching between the meta-biomaterial and the host tissue is one of the primary considerations for bone scaffolds, there is a need for computational models that offer the relationship between geometrical designs and the resulting properties of meta-biomaterials. The growth of literature addressing these key limitations are critical in taking meta-biomaterial research into clinical practice.

5. Conclusion

Auxetic materials are metamaterials with unusual properties that originate from their geometrical architecture. This concept has been explored in the context of CoCrMo additively manufactured bone scaffolds with different negative Poisson's ratio ($-\upsilon$). In particular, the paper demonstrates the use of laser-powder bed fusion (L-PBF) to fabricate porous auxetic CoCrMo bone scaffolds and reports the design, processing parameters, print quality and multi-criteria decision-making for the first time. The study revealed five auxetic architectures (AX1-AX5) for the design of load-bearing meta-biomaterial offering a υ of -0.1 to -0.24 at a porosity range of 73–82% mimicking the requirement for a critical size bone scaffold. The results found Ashby's criterion to be limited in predicting the performance of auxetic bio-material scaffolds due to the complex pore geometries. Although SEM analysis on the L-PBF processed scaffolds identified dimensional inaccuracies, overall variation in porosity was found to be limited to 5.8% lower in comparison to the ideal design. Tensile tests revealed that the L-PBF processed CoCrMo bulk material featured Young's modulus, yield strength and ultimate tensile strength of 194.23 GPa, 975.6 MPa and 1169.81 MPa, respectively consistent with the literature confirming the suitability of the process parameters used. Compressive tests on the CoCrMo auxetic meta-biomaterials showed elastic modulus and compressive strength in the range of 1.13–1.66 GPa and 32–56 MPa, respectively with the highest and lowest performance for AX1 and AX2. When it comes to failure modes, localised and catastrophic failures influenced by both the unit cell shape and the L-PBF process were observed. Considering the range of performances observed for the meta-biomaterials, a decision-making procedure for auxetic bone scaffolds featuring five selection criteria in the order Poisson's ratio > Porosity > yield strength > elastic modulus > ease of design applied to two scenarios to identify ideal designs are also demonstrated. The combined AHP and TOPSIS method found AX4 and AX1 as the best scaffold design to offer a near-zero and highest $-\upsilon$, respectively while satisfying the relative importance of five other parameters relevant for meta-biomaterials. The methodology demonstrated in this study can be adopted to systematically conceive and select suitable auxetic meta-biomaterial bone scaffolds that offer targeted $-\upsilon$ while maintaining high porosity.

CRediT authorship contribution statement

Chameekara T. Wanniarachchi: Writing – review & editing, Writing – original draft, Visualization, Validation, Software, Methodology, Investigation, Formal analysis, Conceptualization. **Arun Arjunan:** Writing – review & editing, Writing – original draft, Visualization, Validation, Supervision, Software, Methodology, Investigation, Funding acquisition, Formal analysis, Conceptualization. **Ahmad Baroutaji:** Writing – review & editing, Writing – original draft, Visualization, Validation, Supervision, Software, Methodology, Investigation, Formal analysis, Conceptualization. **Manpreet Singh:** Visualization, Validation, Software, Investigation.

Declaration of competing interest

The authors declare that they have no known competing financial interests or personal relationships that could have appeared to influence the work reported in this paper.

Data availability

Data will be made available on request.

References

Abdelaal, O., Darwish, S., 2012. Analysis, fabrication and a biomedical application of auxetic cellular structures. Int. J. Eng. Innov. Technol. 2, 218–223.
Ada Steponavičiūtė, A. Šlivinskas, G. Mordas, G. Račiukaitis, Characterization and Performance of CoCrMo Powder for Additive Manufacturing, (n.d.) vol. 1.
Ahmed, A., Majeed, A., Atta, Z., Guozhu, G., 2019. Dimensional quality and distortion analysis of thin-walled alloy parts of AlSi10Mg manufactured by selective laser melting. J. Manuf. Mater. Process. 3, 51. https://doi.org/10.3390/jmmp3020051.
Alomarah, A., Ruan, D., Masood, S., 2018. Tensile properties of an auxetic structure with re-entrant and chiral features—a finite element study. Int. J. Adv. Manuf. Technol. 99, 2425–2440. https://doi.org/10.1007/s00170-018-2637-y.

Arjunan, A., Singh, M., Baroutaji, A., Wang, C., 2020a. Additively manufactured AlSi10Mg inherently stable thin and thick-walled lattice with negative Poisson's ratio. Compos. Struct. 247, 112469 https://doi.org/10.1016/j.compstruct.2020.112469.

Arjunan, A., Demetriou, M., Baroutaji, A., Wang, C., 2020b. Mechanical performance of highly permeable laser melted Ti6Al4V bone scaffolds. J. Mech. Behav. Biomed. Mater. 102, 103517 https://doi.org/10.1016/j.jmbbm.2019.103517.

Arjunan, A., Baroutaji, A., Praveen, A.S., Robinson, J., Wang, C., 2020c. Classification of biomaterial functionality. In: Ref. Modul. Mater. Sci. Mater. Eng. Elsevier. https://doi.org/10.1016/B978-0-12-815732-9.00027-9.

Arjunan, A., Zahid, S., Baroutaji, A., Robinson, J., 2020d. 3D printed auxetic nasopharyngeal swabs for COVID-19 sample collection. J. Mech. Behav. Biomed. Mater., 104175 https://doi.org/10.1016/j.jmbbm.2020.104175.

Arjunan, A., Robinson, J., Al Ani, E., Heaselgrave, W., Baroutaji, A., Wang, C., 2020e. Mechanical performance of additively manufactured pure silver antibacterial bone scaffolds. J. Mech. Behav. Biomed. Mater. 112, 104090 https://doi.org/10.1016/j.jmbbm.2020.104090.

Arjunan, A., Robinson, J., Baroutaji, A., Tuñón-Molina, A., Martí, M., Serrano-Aroca, Á., 2021a. 3D printed cobalt-chromium-molybdenum porous superalloy with superior antiviral activity. Int. J. Mol. Sci. 22 https://doi.org/10.3390/ijms222312721.

Arjunan, A., Baroutaji, A., Robinson, J., Praveen, A.S., Pollard, A., Wang, C., 2021b. Future directions and requirements for tissue engineering biomaterials. In: Ref. Modul. Mater. Sci. Mater. Eng. Elsevier. https://doi.org/10.1016/B978-0-12-815732-9.00068-1.

Ashby, M.F., 2006. The properties of foams and lattices. Philos. Trans. R. Soc. A Math. Phys. Eng. Sci. 364, 15–30. https://doi.org/10.1098/rsta.2005.1678.

Baker, C.E., 2013. Auxetic spinal implants: consideration of negative Poisson's ratio in the design of an artificial intervertebral disc. J. Chem. Inf. Model. 53, 1689–1699. https://doi.org/10.1017/CBO9781107415324.004.

Barbas, A., Bonnet, A.-S.S., Lipinski, P., Pesci, R., Dubois, G., 2012. Development and mechanical characterization of porous titanium bone substitutes. J. Mech. Behav. Biomed. Mater. 9, 34–44. https://doi.org/10.1016/j.jmbbm.2012.01.008.

Bari, K., Arjunan, A., 2019. Extra low interstitial titanium based fully porous morphological bone scaffolds manufactured using selective laser melting. J. Mech. Behav. Biomed. Mater. 95, 1–12. https://doi.org/10.1016/j.jmbbm.2019.03.025.

Baroutaji, A., Arjunan, A., Niknejad, A., Tran, T., Olabi, A.-G., 2019. Application of cellular material in crashworthiness applications: an overview. In: Ref. Modul. Mater. Sci. Mater. Eng. Elsevier. https://doi.org/10.1016/B978-0-12-803581-8.09268-7.

Baroutaji, A., Arjunan, A., Robinsion, J., Ramadan, M., Abdelkareem, M.A., Olabi, A.-G., 2022. Metallic meta-biomaterial as biomedical implants. In: Olabi, A.-G. (Ed.), Encycl. Smart Mater. Elsevier, Oxford, pp. 70–80. https://doi.org/10.1016/B978-0-12-815732-9.00117-0.

Bauer, J., Hengsbach, S., Tesari, I., Schwaiger, R., Kraft, O., 2014. High-strength cellular ceramic composites with 3D microarchitecture. Proc. Natl. Acad. Sci. U.S.A. 111, 2453–2458. https://doi.org/10.1073/pnas.1315147111.

Behl, B., Papageorgiou, I., Brown, C., Hall, R., Tipper, J.L., Fisher, J., Ingham, E., 2013. Biological effects of cobalt-chromium nanoparticles and ions on dural fibroblasts and dural epithelial cells. Biomaterials 34, 3547–3558. https://doi.org/10.1016/j.biomaterials.2013.01.023.

Benedetti, M., Klarin, J., Johansson, F., Fontanari, V., Luchin, V., Zappini, G., Molinari, A., 2019. Study of the compression behaviour of Ti6Al4V trabecular structures produced by additive laser manufacturing. Materials 12. https://doi.org/10.3390/ma12091471.

Berdie, A.D., Osaci, M., Muscalagiu, I., Barz, C., 2017. A combined approach of AHP and TOPSIS methods applied in the field of integrated software systems. IOP Conf. Ser. Mater. Sci. Eng. 200 https://doi.org/10.1088/1757-899X/200/1/012041.

Bertoldi, K., Vitelli, V., Christensen, J., Van Hecke, M., 2017. Flexible mechanical metamaterials. Nat. Rev. Mater. 2 https://doi.org/10.1038/natrevmats.2017.66.

Bertolini, M., Esposito, G., Romagnoli, G., 2020. A TOPSIS-based approach for the best match between manufacturing technologies and product specifications. Expert Syst. Appl. 159, 113610 https://doi.org/10.1016/j.eswa.2020.113610.

Bordin, A., Ghiotti, A., Bruschi, S., Facchini, L., Bucciotti, F., 2014. Machinability characteristics of wrought and EBM CoCrMo alloys. Procedia CIRP 14, 89–94. https://doi.org/10.1016/j.procir.2014.03.082.

BSI, 2016. Bsi. ISO 6892-1:2016 - Tensile testing Part 1 : Method of test at room temperature.

Chen, J., Hou, W., Wang, X., Chu, S., Yang, Z., 2019. Microstructure, porosity and mechanical properties of selective laser melted AlSi10Mg. Chin. J. Aeronaut. https://doi.org/10.1016/j.cja.2019.08.017.

Choi, H.J., Lee, J.J., Park, Y.J., Shin, J.-W., Sung, H.-J.J., Shin, J.-W., Wu, Y., Kim, J.K., 2016. MG-63 osteoblast-like cell proliferation on auxetic PLGA scaffold with mechanical stimulation for bone tissue regeneration. Biomater. Res. 20, 33. https://doi.org/10.1186/s40824-016-0080-4.

Choi, M.-J., Kang, S.-H., Oh, M.-H., Cho, S., 2019. Controllable optimal design of auxetic structures for extremal Poisson's ratio of −2. Compos. Struct. 226, 111215 https://doi.org/10.1016/J.COMPSTRUCT.2019.111215.

Ciurana, J., Hernandez, L., Delgado, J., 2013. Energy density analysis on single tracks formed by selective laser melting with CoCrMo powder material. Int. J. Adv. Manuf. Technol. 68, 1103–1110. https://doi.org/10.1007/s00170-013-4902-4.

Cornacchia, G., Cecchel, S., Battini, D., Petrogalli, C., Avanzini, A., 2021. Microstructural, mechanical, and tribological characterization of selective laser melted CoCrMo alloy under different heat treatment conditions and hot isostatic pressing. Adv. Eng. Mater. https://doi.org/10.1002/adem.202100928, 2100928.

Davoodi, E., Montazerian, H., Mirhakimi, A.S., Zhianmanesh, M., Ibhadode, O., Shahabad, S.I., Esmaeilizadeh, R., Sarikhani, E., Toorandaz, S., Sarabi, S.A., Nasiri, R., Zhu, Y., Kadkhodapour, J., Li, B., Khademhosseini, A., Toyserkani, E., 2022. Additively manufactured metallic biomaterials. Bioact. Mater. 15, 214–249. https://doi.org/10.1016/j.bioactmat.2021.12.027.

de Terris, T., Andreau, O., Peyre, P., Adamski, F., Koutiri, I., Gorny, C., Dupuy, C., 2019. Optimization and comparison of porosity rate measurement methods of Selective Laser Melted metallic parts. Addit. Manuf. 28, 802–813. https://doi.org/10.1016/j.addma.2019.05.035.

Dobrzański, L.A., Reimann, Ł., 2011. Influence of Cr and Co on hardness and corrosion resistance CoCrMo alloys used on dentures. J. Achiev. Mater. Manufaturing Eng. 49, 193–199.

Dohale, V., Akarte, M., Gupta, S., Verma, V., 2021. Additive manufacturing process selection using MCDM. Lect. Notes Mech. Eng. 601–609. https://doi.org/10.1007/978-981-15-3639-7_72.

Dolgov, A., N, Dikova, T., Dzhendov, D., Pavlova, D., Simov, M., 2016. Mechanical properties of dental Co-Cr alloys fabricated via casting and selective laser melting. Sci. Proc. Ii Int. Sci. Conf. "Innovations Eng. 33, 29–33, 2016.

Dong, Z., Zhang, X., Shi, W., Zhou, H., Lei, H., Liang, J., 2018. Study of size effect on microstructure and mechanical properties of AlSi10Mg samples made by selective laser melting. Materials 11. https://doi.org/10.3390/ma11122463.

dos Santos, C., Habibe, A.F., Simba, B.G., Lins, J.F.C., de Freitas, B.X., Nunes, C.A., 2020. CoCrMo-base alloys for dental applications obtained by selective laser melting (slm) and cad/cam milling. Mater. Res. 23, 1–6. https://doi.org/10.1590/1980-5373-MR-2019-0599.

Echeta, I., Feng, X., Dutton, B., Leach, R., Piano, S., 2020. Review of defects in lattice structures manufactured by powder bed fusion. Int. J. Adv. Manuf. Technol. 106, 2649–2668. https://doi.org/10.1007/s00170-019-04753-4.

Emovon, I., Oghenenyerovwho, O.S., 2020. Application of MCDM method in material selection for optimal design: a review. Results Mater 7, 100115. https://doi.org/10.1016/j.rinma.2020.100115.

Evans, K.E., 1991. Auxetic polymers: a new range of materials. Endeavour 15, 170–174. https://doi.org/10.1016/0160-9327(91)90123-S.

Ganjian, M., Janbaz, S., van Manen, T., Tümer, N., Modaresifar, K., Minneboo, M., Fratila-Apachitei, L.E., Zadpoor, A.A., 2022. Controlled metal crumpling as an alternative to folding for the fabrication of nanopatterned meta-biomaterials. Mater. Des. 220, 110844 https://doi.org/10.1016/j.matdes.2022.110844.

Genovese, K., Leeflang, S., Zadpoor, A.A., 2017. Microscopic full-field three-dimensional strain measurement during the mechanical testing of additively manufactured porous biomaterials. J. Mech. Behav. Biomed. Mater. 69, 327–341. https://doi.org/10.1016/j.jmbbm.2017.01.010.

Hadadzadeh, A., Shalchi Amirkhiz, B., Odeshi, A., Li, J., Mohammadi, M., 2019. Role of hierarchical microstructure of additively manufactured AlSi10Mg on dynamic loading behavior. Addit. Manuf. 28, 1–13. https://doi.org/10.1016/J.ADDMA.2019.04.012.

Han, S.C., Kang, D.S., Kang, K., 2019. Two nature-mimicking auxetic materials with potential for high energy absorption. Mater. Today 26, 30–39. https://doi.org/10.1016/j.mattod.2018.11.004.

Hazlehurst, K.B., 2014. The Adoption of Laser Melting Technology for the Manufacture of Functionally Graded Cobalt Chrome Alloy Femoral Stems.

Hazlehurst, K.B., Wang, C.J., Stanford, M., 2014. An investigation into the flexural characteristics of functionally graded cobalt chrome femoral stems manufactured using selective laser melting. Mater. Des. 60, 177–183. https://doi.org/10.1016/j.matdes.2014.03.068.

Hendrikson, W.J., van Blitterswijk, C.A., Rouwkema, J., Moroni, L., 2017. The use of finite element analyses to design and fabricate three-dimensional scaffolds for skeletal tissue engineering. Front. Bioeng. Biotechnol. 5, 30. https://doi.org/10.3389/fbioe.2017.00030.

Hoffmeister, B.K., Smith, S.R., Handley, S.M., Rho, J.Y., 2000. Anisotropy of Young's modulus of human tibial cortical bone. Med. Biol. Eng. Comput. 38, 333–338. http://www.ncbi.nlm.nih.gov/pubmed/10912351. (Accessed 9 August 2019). accessed.

International Organization for Standardization, 2011. ISO 13314:2011 Mechanical testing of metals – ductility testing – compression test for porous and cellular metals (ISO Standard No. 13314:2011(E)). Int. Organ. Stand. 2011, 1–7.

INTERNATIONAL STANDARD Verification of Static Uniaxial Testing — Calibration and Verification of the, 2018, p. 2018.

Jiang, Y., Li, Y., 2018. 3D printed auxetic mechanical metamaterial with chiral cells and Re-entrant cores. Sci. Rep. 8, 2397. https://doi.org/10.1038/s41598-018-20795-2.

Jiang, Y., Rudra, B., Shim, J., Li, Y., 2019. Limiting strain for auxeticity under large compressive Deformation: chiral vs. re-entrant cellular solids. Int. J. Solid Struct. 162, 87–95. https://doi.org/10.1016/J.IJSOLSTR.2018.11.035.

Jin, Y., Xie, C., Gao, Q., Zhou, X., Li, G., Du, J., He, Y., 2021. Fabrication of multi-scale and tunable auxetic scaffolds for tissue engineering. Mater. Des. 197, 109277 https://doi.org/10.1016/j.matdes.2020.109277.

Joseph, A., Mahesh, V., Harursampath, D., 2021. On the application of additive manufacturing methods for auxetic structures: a review. Adv. Manuf. 9, 342–368. https://doi.org/10.1007/s40436-021-00357-y.

Kan, W.H., Nadot, Y., Foley, M., Ridosz, L., Proust, G., Cairney, J.M., 2019. Factors that affect the properties of additively-manufactured AlSi10Mg: porosity versus microstructure. Addit. Manuf. 29, 100805 https://doi.org/10.1016/J.ADDMA.2019.100805.

Kang, Y., Chang, J., 2018. Channels in a porous scaffold: a new player for vascularization, Regen. Med 13, 705–715. https://doi.org/10.2217/rme-2018-0022.

Kim, Y., Son, K.H., Lee, J.W., 2021. Auxetic structures for tissue engineering scaffolds and biomedical devices. Materials 14. https://doi.org/10.3390/ma14226821.

Kluyskens, L., Debieux, P., Wong, K.L., Krych, A.J., Saris, D.B.F., 2022. Biomaterials for meniscus and cartilage in knee surgery: state of the art. J. ISAKOS. 7, 67–77. https://doi.org/10.1136/jisakos-2020-000600.

Kolken, H.M.A.M.A., Zadpoor, A.A., 2017. Auxetic Mechanical Metamaterials. Royal Society of Chemistry. http://xlink.rsc.org/?DOI=C6RA27333E. (Accessed 19 September 2019). accessed.

Kolken, H.M.A., Lietaert, K., van der Sloten, T., Pouran, B., Meynen, A., Van Loock, G., Weinans, H., Scheys, L., Zadpoor, A.A., 2020. Mechanical performance of auxetic meta-biomaterials. J. Mech. Behav. Biomed. Mater. 104 https://doi.org/10.1016/j.jmbbm.2020.103658.

Kolken, H.M.A., Callens, S.J.P., Leeflang, M.A., Mirzaali, M.J., Zadpoor, A.A., 2022a. Merging strut-based and minimal surface meta-biomaterials: decoupling surface area from mechanical properties. Addit. Manuf. 52, 102684 https://doi.org/10.1016/j.addma.2022.102684.

Kolken, H.M.A., Garcia, A.F., Du Plessis, A., Meynen, A., Rans, C., Scheys, L., Mirzaali, M. J., Zadpoor, A.A., 2022b. Mechanisms of fatigue crack initiation and propagation in auxetic meta-biomaterials. Acta Biomater. 138, 398–409. https://doi.org/10.1016/j.actbio.2021.11.002.

Lekesiz, H., Bhullar, S.K., Karaca, A.A., Jun, M.B.G., 2017. Mechanical characterization of auxetic stainless steel thin sheets with reentrant structure. Smart Mater. Struct. 26, 085022 https://doi.org/10.1088/1361-665X/aa73a4.

Li, N., Huang, S., Zhang, G., Qin, R., Liu, W., Xiong, H., Shi, G., Blackburn, J., 2019. Progress in additive manufacturing on new materials: a review. J. Mater. Sci. Technol. 35, 242–269. https://doi.org/10.1016/J.JMST.2018.09.002.

Liu, M., Takata, N., Suzuki, A., Kobashi, M., 2019. Development of gradient microstructure in the lattice structure of AlSi10Mg alloy fabricated by selective laser melting. J. Mater. Sci. Technol. https://doi.org/10.1016/J.JMST.2019.06.015.

Maamoun, A.H., Xue, Y.F., Elbestawi, M.A., Veldhuis, S.C., Maamoun, A.H., Xue, Y.F., Elbestawi, M.A., Veldhuis, S.C., 2018. Effect of selective laser melting process parameters on the quality of Al alloy parts: powder characterization, density, surface roughness, and dimensional accuracy. Materials 11, 2343. https://doi.org/10.3390/ma11122343.

Mahbod, M., Asgari, M., 2019. Elastic and plastic characterization of a new developed additively manufactured functionally graded porous lattice structure: analytical and numerical models. Int. J. Mech. Sci. 155, 248–266. https://doi.org/10.1016/J.IJMECSCI.2019.02.041.

Mantrala, K.M., Das, M., Balla, V.K., Rao, C.S., Kesava Rao, V.V.S., 2015. Additive manufacturing of Co-Cr-Mo alloy: influence of heat treatment on microstructure, tribological, and electrochemical properties. Front. Mech. Eng. 1 https://doi.org/10.3389/fmech.2015.00002.

Mardling, P., Alderson, A., Jordan-Mahy, N., Le Maitre, C.L., 2020. The use of auxetic materials in tissue engineering. Biomater. Sci. 8 https://doi.org/10.1039/C9BM01928F, 2074–2083.

Milan, J.L., Planell, J.A., Lacroix, D., 2010. Simulation of bone tissue formation within a porous scaffold under dynamic compression. Biomech. Model. Mechanobiol. 9, 583–596. https://doi.org/10.1007/s10237-010-0199-5.

Mirzaali, M.J., Caracciolo, A., Pahlavani, H., Janbaz, S., Vergani, L., Zadpoor, A.A., 2018. Multi-material 3D printed mechanical metamaterials: rational design of elastic properties through spatial distribution of hard and soft phases. Appl. Phys. Lett. 113, 241903 https://doi.org/10.1063/1.5064864.

Mirzaali, M.J., Pahlavani, H., Zadpoor, A.A., 2019. Auxeticity and stiffness of random networks: lessons for the rational design of 3D printed mechanical metamaterials. Appl. Phys. Lett. 115, 021901 https://doi.org/10.1063/1.5096590.

Mizzi, L., Attard, D., Gatt, R., Pozniak, A.A., Wojciechowski, K.W., Grima, J.N., 2015. Influence of Translational Disorder on the Mechanical Properties of Hexachiral Honeycomb Systems. https://doi.org/10.1016/j.compositesb.2015.04.057.

Mohamed, S.R., Ghani, S.A.C., Sawangsri, W., 2019. Mechanical properties of additive manufactured cocrmo meta-biomaterials for load bearing implants. J. Tribol. 21, 93–107.

Monroy, K., Delgado, J., Ciurana, J., 2013. Study of the pore formation on CoCrMo alloys by selective laser melting manufacturing process. Procedia Eng. 63, 361–369. https://doi.org/10.1016/j.proeng.2013.08.227.

Mp, C.C., Performance, M.P., Original, E.O.S., Set, P., M, P., Surface, M.P. Performance, 2011. Material Data Sheet EOS CobaltChrome MP1 Material Data Sheet Technical Data, vol. 49, pp. 1–6.

Nečemer, B., Kramberger, J., Vuherer, T., Glodež, S., 2019. Fatigue crack initiation and propagation in re-entrant auxetic cellular structures. Int. J. Fatig. 126, 241–247. https://doi.org/10.1016/J.IJFATIGUE.2019.05.010.

Ngiam, M., Liao, S., Ong Jun Jie, T., Sui, Xiaodi, Dong, Yixiang, Ramakrishna, S., Chan, C.K., 2010. Effects of mechanical stimulation in osteogenic differentiation of bone marrow-derived mesenchymal stem cells on aligned nanofibrous scaffolds. Http://Dx.Doi.Org/10.1177/0883911510393162. 26. https://doi.org/10.1177/0883911510393162, 56–70.

Nikkhah, H., Baroutaji, A., Olabi, A.G., 2019. Crashworthiness design and optimisation of windowed tubes under axial impact loading. Thin-Walled Struct. 142, 132–148. https://doi.org/10.1016/j.tws.2019.04.052.

Park, Y.J., Kim, J.K., 2013. The effect of negative Poisson's ratio polyurethane scaffolds for articular cartilage tissue engineering applications. Adv. Mater. Sci. Eng. 2013 https://doi.org/10.1155/2013/853289.

Perier-Metz, C., Duda, G.N., Checa, S., 2020. Mechano-biological computer model of scaffold-supported bone regeneration: effect of bone graft and scaffold structure on large bone defect tissue patterning. Front. Bioeng. Biotechnol. 8, 1–15. https://doi.org/10.3389/fbioe.2020.585799.

Pham, N.H., Voronov, R.S., Vangordon, S.B., Sikavitsas, V.I., V Papavassiliou, D., 2012. Predicting the stress distribution within scaffolds with ordered architecture. Biorheology 49, 235–247. https://doi.org/10.3233/BIR-2012-0613.

Pleass, C., Jothi, S., 2018. Influence of powder characteristics and additive manufacturing process parameters on the microstructure and mechanical behaviour of Inconel 625 fabricated by Selective Laser Melting. Addit. Manuf. 24, 419–431. https://doi.org/10.1016/j.addma.2018.09.023.

Rahim, R., Supiyandi, S., Siahaan, A.P.U., Listyorini, T., Utomo, A.P., Triyanto, W.A., Irawan, Y., Aisyah, S., Khairani, M., Sundari, S., Khairunnisa, K., 2018. TOPSIS method application for decision support system in internal control for selecting best employees. J. Phys. Conf. Ser. 1028 https://doi.org/10.1088/1742-6596/1028/1/012052.

Rahmani, R., Kamboj, N., Brojan, M., Antonov, M., Prashanth, K.G., 2022. Hybrid metal-ceramic biomaterials fabricated through powder bed fusion and powder metallurgy for improved impact resistance of craniofacial implants. Materialia 24, 101465. https://doi.org/10.1016/j.mtla.2022.101465.

Raigar, J., Sharma, V.S., Srivastava, S., Chand, R., Singh, J., 2020. A decision support system for the selection of an additive manufacturing process using a new hybrid MCDM technique. Sadhana - Acad. Proc. Eng. Sci. 45 https://doi.org/10.1007/s12046-020-01338-w.

Read, N., Wang, W., Essa, K., Attallah, M.M., 2015. Selective laser melting of AlSi10Mg alloy. Process optimisation and mechanical properties development 65, 417–424. https://doi.org/10.1016/j.matdes.2014.09.044.

Rho, J., Ashman, R., Turner, C., 1993. Young's modulus of trabecular and cortical bone material: ultrasonic and microtensile measurements. J. Biomech. 26, 111–119. https://doi.org/10.1016/0021-9290(93)90042-D.

Robinson, J., Stanford, M., Arjunan, A., 2020a. Stable formation of powder bed laser fused 99.9% silver. Mater. Today Commun., 101195 https://doi.org/10.1016/j.mtcomm.2020.101195.

Robinson, J., Stanford, M., Arjunan, A., 2020b. Correlation between selective laser melting parameters, pore defects and tensile properties of 99.9% silver. Mater. Today Commun. 25, 101550 https://doi.org/10.1016/j.mtcomm.2020.101550.

Robinson, J., Arjunan, A., Baroutaji, A., Martí, M., Tuñón Molina, A., Serrano-Aroca, Á., Pollard, A., 2021. Additive manufacturing of anti-SARS-CoV-2 Copper-Tungsten-Silver alloy. Rapid Prototyp. J. https://doi.org/10.1108/RPJ-06-2021-0131 ahead-of-.

Roszkowska, E., 2011. Multi-criteria decision making models by applying the topsis method to crisp and interval data. Interface Sci. J. 6, 200–230.

Sabaghi, M., Mascle, C., Baptiste, P., 2015. Application of DOE-TOPSIS technique in decision-making problems. IFAC-PapersOnLine 28, 773–777. https://doi.org/10.1016/j.ifacol.2015.06.176.

Sapti, M., 2019. A textbook on fundamentals and applications of nanotechnology. Kemamp. Koneksi Mat. (Tinjauan Terhadap Pendekatan Pembelajaran Savi). 53, 1689–1699.

Scarpa, F., 2008. Auxetic materials for bioprostheses. IEEE Signal Process. Mag. 25 https://doi.org/10.1109/MSP.2008.926663.

Scheu, C., Kaplan, W.D., 2012. Introduction to scanning electron microscopy. In-Situ Electron Microsc. Appl. Physics, Chem. Mater. Sci. 1–37. https://doi.org/10.1002/9783527652167.ch1.

Singh, R., Lee, P.D., Lindley, T.C., Kohlhauser, C., Hellmich, C., Bram, M., Imwinkelried, T., Dashwood, R.J., 2010. Characterization of the deformation behavior of intermediate porosity interconnected Ti foams using micro-computed tomography and direct finite element modeling. Acta Biomater. 6, 2342–2351. https://doi.org/10.1016/j.actbio.2009.11.032.

Soman, P., Fozdar, D.Y., Lee, J.W., Phadke, A., Varghese, S., Chen, S., 2012. A three-dimensional polymer scaffolding material exhibiting a zero Poisson's ratio. Soft Matter 8, 4946–4951. https://doi.org/10.1039/c2sm07354d.

Soro, N., Attar, H., Wu, X., Dargusch, M.S., 2019. Investigation of the structure and mechanical properties of additively manufactured Ti-6Al-4V biomedical scaffolds designed with a Schwartz primitive unit-cell. Mater. Sci. Eng. 745, 195–202. https://doi.org/10.1016/j.msea.2018.12.104.

Spagnoli, A., Brighenti, R., Lanfranchi, M., Soncini, F., 2015. On the Auxetic Behaviour of Metamaterials with Re-entrant Cell Structures. https://www.sciencedirect.com/science/article/pii/S187770581501214X. (Accessed 19 September 2019). accessed.

Tan, J.H., Wong, W.L.E., Dalgarno, K.W., 2017. An overview of powder granulometry on feedstock and part performance in the selective laser melting process. Addit. Manuf. 18, 228–255. https://doi.org/10.1016/j.addma.2017.10.011.

Tolochko, N.K., Savich, V.V., Laoui, T., Froyen, L., Onofrio, G., Signorelli, E., Titov, V.I., 2002. Dental root implants produced by the combined selective laser sintering/melting of titanium powders. Proc. Inst. Mech. Eng. Part L J. Mater. Des. Appl. 216, 267–270. https://doi.org/10.1243/146442002760387952.

Vance, A., Bari, K., Arjunan, A., 2019. Investigation of Ti64 Sheathed Cellular Anatomical Structure as a Tibia Implant, vol. 5, 035008. https://doi.org/10.1088/2057-1976/ab0bd7.

Velasco, M.A., Narváez-Tovar, C.A., Garzón-Alvarado, D.A., 2015. Design, materials, and mechanobiology of biodegradable scaffolds for bone tissue engineering. BioMed Res. Int. 2015 https://doi.org/10.1155/2015/729076.

Vithalani, A.A., Vithalani, C.H., 2017. Application of combined TOPSIS and AHP method for spectrum selection in cognitive radio by channel characteristic evaluation. Int. J. Electron. Commun. Eng. 10, 71–79.

Wang, T., Wang, L., Ma, Z., Hulbert, G.M., 2018. Elastic analysis of auxetic cellular structure consisting of re-entrant hexagonal cells using a strain-based expansion homogenization method. Mater. Des. 160, 284–293. https://doi.org/10.1016/J.MATDES.2018.09.013.

Warner, J.J., Gillies, A.R., Hwang, H.H., Zhang, H., Lieber, R.L., Chen, S., 2017. 3D-printed biomaterials with regional auxetic properties. J. Mech. Behav. Biomed. Mater. 76, 145–152. https://doi.org/10.1016/j.jmbbm.2017.05.016.

Weißmann, V., Drescher, P., Bader, R., Seitz, H., Hansmann, H., Laufer, N., 2017. Comparison of Single Ti 6 Al 4 V Struts Made Using Selective Laser Melting and Electron Beam Melting Subject to Part Orientation. Basel), Metals. https://doi.org/10.3390/met7030091.

Williams, J.L., Lewis, J.L., 1982. Properties and an anisotropic model of cancellous bone from the proximal tibial epiphysis. J. Biomech. Eng. 104, 50–56. https://doi.org/10.1115/1.3138303.

Wojciechowski, K.W., 1987. Constant thermodynamic tension Monte Carlo studies of elastic properties of a two-dimensional system of hard cyclic hexamers. Mol. Phys. 61, 1247–1258. https://doi.org/10.1080/00268978700101761.

Wojciechowski, K.W., 1989. Two-dimensional isotropic system with a negative Poisson ratio. Phys. Lett. 137, 60–64. https://doi.org/10.1016/0375-9601(89)90971-7.

Wojciechowski, K.W., 2003. Remarks on "Poisson ratio beyond the limits of the elasticity theory. J. Phys. Soc. Japan. 72, 1819–1820. https://doi.org/10.1143/JPSJ.72.1819.

Yakout, M., Elbestawi, M.A., Veldhuis, S.C., 2019. Density and mechanical properties in selective laser melting of Invar 36 and stainless steel 316L. J. Mater. Process. Technol. 266, 397–420. https://doi.org/10.1016/J.JMATPROTEC.2018.11.006.

Yan, C., Hao, L., Hussein, A., Bubb, S.L., Young, P., Raymont, D., 2014. Evaluation of light-weight AlSi10Mg periodic cellular lattice structures fabricated via direct metal laser sintering. J. Mater. Process. Technol. 214, 856–864. https://doi.org/10.1016/J.JMATPROTEC.2013.12.004.

Yang, S., Leong, K.-F., Du, Z., Chua, C.-K., 2002. The design of scaffolds for use in tissue engineering. Part II. Rapid prototyping techniques. Tissue Eng. 8, 1–11. https://doi.org/10.1089/107632702753503009.

Yang, H., Wang, B., Ma, L., 2019. Mechanical properties of 3D double-U auxetic structures. Int. J. Solid Struct. 180–181, 13–29. https://doi.org/10.1016/j.ijsolstr.2019.07.007.

Yazdani, M., Payam, A.F., 2015. A comparative study on material selection of microelectromechanical systems electrostatic actuators using Ashby, VIKOR and TOPSIS. Mater. Des. 65, 328–334. https://doi.org/10.1016/j.matdes.2014.09.004.

Yu, T., Hyer, H., Sohn, Y., Bai, Y., Wu, D., 2019. Structure-property relationship in high strength and lightweight AlSi10Mg microlattices fabricated by selective laser melting. Mater. Des. 182, 108062 https://doi.org/10.1016/J.MATDES.2019.108062.

Zadpoor, A.A.A.A., 2017. Mechanics of Additively Manufactured Biomaterials. Elsevier Ltd. https://doi.org/10.1016/j.jmbbm.2017.03.018.

Zadpoor, A.A., 2020. Meta-biomaterials. Biomater. Sci. 8, 18–38. https://doi.org/10.1039/c9bm01247h.

Zhang, D., Xiao, J., Yu, W., Guo, Q., Yang, J., 2018. Hierarchical metal/polymer metamaterials of tunable negative Poisson's ratio fabricated by initiator-integrated 3D printing (i3DP). Nanotechnology 29, 505704. https://doi.org/10.1088/1361-6528/aae283.

Zhang, J., Lu, G., You, Z., 2020. Large deformation and energy absorption of additively manufactured auxetic materials and structures: a review. Compos. B Eng. 201, 108340 https://doi.org/10.1016/j.compositesb.2020.108340.

Zhang, K., Ma, B., Hu, K., Yuan, B., Sun, X., Song, X., Tang, Z., Lin, H., Zhu, X., Zheng, Y., García, A.J., Mikos, A.G., Anderson, J.M., Zhang, X., 2022a. Evidence-based biomaterials research. Bioact. Mater. 15, 495–503. https://doi.org/10.1016/j.bioactmat.2022.04.014.

Zhang, L., Lee, W., Li, X., Jiang, Y., Fang, N.X., Dai, G., Liu, Y., 2022b. 3D direct printing of mechanical and biocompatible hydrogel meta-structures. Bioact. Mater. 10, 48–55. https://doi.org/10.1016/j.bioactmat.2021.08.015.

Zysset, P.K., Edward Guo, X., Edward Hoffler, C., Moore, K.E., Goldstein, S.A., 1999. Elastic modulus and hardness of cortical and trabecular bone lamellae measured by nanoindentation in the human femur. J. Biomech. 32, 1005–1012. https://doi.org/10.1016/S0021-9290(99)00111-6.